# Can aerosols influence deep tropical convection? Aerosol indirect effects in the Hector island thunderstorm

Paul. J. Connolly[a]*, G. Vaughan[a], P.T. May[b], C. Chemel[c], G. Allen[a], T. W. Choularton[a], M. W. Gallagher[a], K. N. Bower[a], J. Crosier[a], C. Dearden[a]

[a]*School of Earth, Atmospheric and Environmental Sciences, The University of Manchester, UK*
[b]*Centre for Australian Weather and Climate Research—A partnership between the Bureau of Meteorology and CSIRO*
[c]*NCAS-Weather, Centre for Atmospheric & Instrumentation Research, University of Hertfordshire, UK*
*Correspondence to: School of Earth, Atmospheric and Environmental Sciences, The University of Manchester, UK.
E-mail: p.connolly@manchester.ac.uk

**This paper addresses the effects of cloud condensation nuclei on the evolution of an intense tropical convective system, known as Hector, using data taken from the Aerosol and Chemical Transport in Tropical Convection (ACTIVE) and Tropical Warm Pool-International Cloud Experiment (TWP-ICE) field campaigns, which were conducted in 2005 and 2006. The Hector thunderstorms were observed in a variety of aerosol conditions so the data serve as an ideal dataset to test whether aerosols have a significant impact on the evolution of convective clouds and precipitation. We find evidence for an aerosol effect on the storm's properties, which are reproduced with a state-of-the-art meso-scale cloud resolving model. Including the measured aerosol concentration within the model is shown to improve the fractions skill score metric for every case presented in the paper, thus giving us confidence that the deep convection observed during the period was indeed influenced by the aerosol entering the storm's inflow. However, we do not find a general relationship for the way aerosols affect properties such as cloud top height, precipitation or radiative properties, as has been suggested in previous work. The reasons for this appear to be because of the non-linearity of interactions between neighbouring cells and because of the variability in the meteorological profiles of temperature, wind and humidity. Copyright © 2011 Royal Meteorological Society**

## 1. Introduction

Intense multicellular cumulonimbus (Cb) like those occurring over the many islands comprising the Maritime Continent of Indonesia and tropical northern Australia are thought to be an important component in the large-scale circulation (Mapes and Houze Jr. 1992). This kind of convection occurs due to the strong diurnal heating cycle, the local topography of the many islands and the prevailing large-scale circulation (Ramage 1968). It is also thought that these storms play a dominant role in the Quasi-Biennial-Oscillation (QBO) (Piani *et al.* 2000); hence they have far reaching consequences.

There are many factors that may affect the intensity of multi-cellular Cb; these range from meteorological factors (e.g. vertical wind shear and humidity structure); and perhaps less well understood, modification of the clouds and their dynamics by the indirect effect of aerosol particles on the cloud microphysics (e.g. Khain *et al.* 2005).

Lohmann and Feichter (2005) identified some possible indirect effects that aerosols may have on clouds. An important indirect effect for mixed phase clouds was

named the 'thermodynamic' indirect effect. In this effect it is hypothesized that increased aerosol loadings result in smaller droplets, which inturn impacts on the ice phase since the population of a subset of aerosols known as Ice Nuclei (IN) are shared amongst a smaller fraction of the cloud and rain drops. Since the droplets that contain IN would be smaller under increased aerosol loadings, the consequence is that less water mass freezes and hence the glaciation of the cloud is suppressed (precipitation from the cloud may also be reduced). This effect was observed in thunderstorms over Texas (Rosenfeld and Woodley 2000), where the cloud contained supercooled liquid water at temperatures as low as $\sim -35°C$; it has also been modelled successfully in a number of studies (Khain *et al.* 2001).

Another effect identified by Lohmann and Feichter's work is the 'riming' indirect effect where it has been hypothesized that smaller cloud droplets reduce the effectiveness of riming. Lohmann *et al.* (2003) found that this effect is not so clear in Arctic clouds; while Connolly *et al.* (2007) found that riming actually *increased* with increased aerosols in deep tropical storms because it allowed for more liquid water to reach higher altitudes in the cloud, where there was more ice. In Connolly *et al.*'s study this led to more precipitation later in the storms lifecycle and apparently worked against the thermodynamic indirect effect. When examining convection downwind of an urban environment, the simulations by van den Heever and Cotton (2007) observed more riming later on in the lifecycle of deep convective storms due to the lofting of more cloud water and through impacts on cold pool forcing; however, they argue that the effects are complex and that non-linear relationships exist between the microphysics and the storm dynamics. Non-linear relationships in a continental storm have also been reported by Ekman *et al.* (2007).

The overall picture from Connolly *et al.*'s study;however, was that 'low' aerosol concentrations (cloud droplet number concentrations of $\sim 100$ cm$^{-3}$) gave rise to more precipitation via warm rain; 'high' aerosol concentrations (cloud droplet number concentrations of $\sim 600$ cm$^{-3}$) resulted in more liquid water at higher altitudes, which then took part in the riming process and resulted in more hail production and precipitation later in the storm life-cycle; and 'intermediate' aerosol concentrations (cloud droplet number concentrations of $\sim 400$ cm$^{-3}$) resulted in the optimal transfer of liquid water to higher altitudes, which then froze rapidly at the threshold temperature for homogeneous freezing of liquid water. This invigorated the updraught through the release of additional latent heat. However, Connolly *et al.*'s study was of a single observed case and used an idealized, 2-D model, so the generality of this result was not confirmed.

In a study assessing the impacts of Saharan dust as Cloud Condensation Nuclei (CCN) in a tropical cyclone, Zhang *et al.* (2007) found that differences in CCN in the range 100–2000 cm$^{-3}$ influenced tropical cyclone development by modifying the hydrometeor properties and therefore spatial distribution of the diabatic heating. Complex dynamical responses resulted in changes in tropical cyclone intensity. van den Heever *et al.* (2006) found that in modelled thunderstorms based on observations from the Cirrus Regional Study of Tropical Anvils and Cirrus Layers-Florida Area Cirrus Experiment (CRYSTAL-FACE) campaign, increasing aerosol concentrations resulted in updrafts that were consistently stronger and anvils covering less spatial area, but with higher condensate mixing ratios. In contrast to these results, Morrison and Grabowski (2011) report on 6 day, 240 member ensemble simulations of aerosol indirect effects in tropical deep convection using a 2-d model and find weaker convection in polluted aerosol conditions which is due to thicker ice clouds being formed near the tropopause and thus radiative heating causing the upper troposphere to be more stable than in the pristine conditions.

There have been many studies addressing the effects of aerosols on convective clouds from a modelling perspective; however, there have been very few studies that veryfy their results against observations. This paper seeks to strengthen the evidence that aerosols do indeed impact on intense convective clouds by comparing model simulations of the aerosol effects on intense convection with observational data taken during the ACTIVE and TWP-ICE field campaigns, which examined cases of an isolated deep convective storm known as 'Hector'. These convective storms occur during the pre-monsoon and monsoon break periods over a group of islands known as the Tiwi Islands (see Figure 1).

This paper builds on the work of May *et al.* (2009), who investigated the Hector thunderstorm (see Section 2). They found that Hector cases observed during 2005 and 2006 with highest aerosol concentrations were associated with lower spatial coverage of rain and more intense updraughts than Hector cases with the lowest aerosol concentrations in the inflow. However, May *et al.* conceded that the cases with the highest aerosol concentrations, which occurred in the pre-monsoon period, were also associated with a drier mid-troposphere. This air could have caused the rain to evaporate and so suppress rainfall coverage. Thus, this study could not show definitively the effect of aerosols on deep convection. May *et al.* (2011) also found evidence of aerosol effects, concluding that they effect the rain-drop size distribution in Hector storms throughout the ACTIVE campaign; they found that the cases with higher aerosol concentrations were associated with broader raindrop size distributions within the storm. Again they suggested that thermodynamic factors still could have been responsible, and suggested that detailed modelling was required to rule out thermodynamic factors, such as the dry mid-troposphere in the pre-monsoon period.

The overall aims of the present study are to use the data collected from the ACTIVE and TWP-ICE campaigns to infer whether aerosol effects were discernible on the precipitation and dynamical properties of Hector. Throughout the paper we will refer to cases with high, medium and low aerosol concentrations as 'High' aerosol, 'medium' aerosol or 'low' aerosol cases. For more information on the ACTIVE and TWP-ICE campaigns the reader is referred to Vaughan *et al.* (2008) and May *et al.* (2008).

## 2. Background to the Hector, island storm

In this study we focus on studying the Hector thunderstorm, over the Tiwi Islands, north of Darwin, Australia. The Hector storms represent some of the deepest convective activity to be found on a regular basis anywhere in the world. The region encompassing the Maritime Continent has been described as the 'boiler box' of the tropics and is the primary area of low-level inflow and high-level outflow for the Hadley and Walker circulations (Keenan *et al.* 1989).

Hector thunderstorms form during the pre-monsoon season (Oct→Dec) and during break periods in the monsoon season (late Dec→April). They occur in the afternoon, their exact location and properties depending on prevailing meteorological conditions (indeed, if the 700 mb wind is too strong or a prominent dry layer is present at middle levels Hector can be suppressed completely, Allen *et al.* 2009).

Carbone *et al.* (2000) presented results of a radar and aircraft study of the sea breeze initiation of Hector during the Maritime Continent Thunderstorm Experiment (MCTEX). They concluded that there are in general two different modes by which Hector develops. The first mode, type 'A' initiation, which is referred to as Nature's back-up mechanism, is quite rare—20% of MCTEX cases—and occurs when convection is suppressed due to low surface / boundary layer humidity; however, strong convection can be initiated when island-scale sea breezes collide near the Tiwi islands' centre. The second mechanism, type 'B' initiation, is much more common (80%) and is a multiple stage forcing involving leeward coast showers that develop small cold pools; these then travel inland when the cold pools become more dense than the marine boundary layer. Typical convergence lines that initiate the convection for these two mechanisms are shown in Figure 1. Large systems result from the westward propagation of squalls that are the product of the merging of small cold pools. These cold pools can also interact with the large island-scale sea breeze or more rarely two gust-fronts from separate parts of the islands can interact. This latter interaction tends to produce the largest Hectors.

Williams *et al.* (1992) classified the storms in this continental regime as being 15-20 km in depth, and having radar reflectivities of typically 30-50 dBZ in the mixed phase region of the storms. Measured Doppler radial velocities were used to estimate the vertical winds as being of the order of 20-40 ms$^{-1}$.

Golding (1993) modelled Hector with a mesoscale model initialized with a morning radiosonde ascent over the islands. Golding reasoned that on many occasions horizontal homogeneity may be assumed over an island and surrounding water at some time in the early morning, since processes initializing and controlling storm development are all local to the island. For this reason, Hectors occurring over the Tiwi Islands have been referred to many times as natural laboratories for studying convection. Wilson *et al.* (2001) argued that a good reason for studying Hector is that it occurs in an environment where day-to-day changes in large-scale conditions are small in magnitude, therefore providing a situation where changes in storm evolution can more easily be isolated and associated with subtle environment changes.

Saito *et al.* (2001) simulated Hectors observed during the MCTEX experiment with a non-hydrostatic model. They found that the diurnal convective activity is not only determined by Convective Available Potential Energy (CAPE) and Convective Inhibition (CIn), but is also quite sensitive to the size of the island, which implies that the local circulation is driven by horizontal pressure gradients. They also found that the topography over the islands, although small, is significant as the lack of any topography delayed convective activity by approximately 30 minutes in their simulations.

They summarized the convection as follows. During the dry stage (no clouds), the sea breeze front (SBF) is driven by the difference in temperature between the land and sea. As expected, the SBF propagates more rapidly from wind-ward coasts than the leeward coasts; however, the head of the density current is deeper at the leeward coast. Rayleigh-Bernard cells develop as do horizontal convective rolls. When the upward motion at the SBF exceeds the lifting condensation level (LCL), clouds start to form (condensation stage). This leads to shallow cumulus (Cu). Eventually, the SBF penetrates further inland with velocities of 7-8 ms$^{-1}$; this is followed by the precipitating Cb stage toward the leeward coasts (for reasons highlighted above). Later in the life cycle the cells tend to merge (merging stage) along an east-west line, corresponding to the major axis of the islands. Vertical wind speeds are greater than 20 ms$^{-1}$ and down-draughts are weak due to lack of dry mid-level environmental air; however, the down-draughts can still generate gust-fronts, which may initiate further convection. Eventually the storm decays (decay stage) due to decreased heating of the land surface.

Crook (2001) performed idealized modelling studies of island thunderstorms finding that one of the non-linearities in such storms is the dependence of the magnitude of convective activity on background flow speed. As the flow speed decreases, the low-level air spends more time over the heat and moisture source provided by the island and therefore the conditional instability at the downwind side of the island is increased. Another important point raised was that low-level moisture is a key determinant to storm strength and timing: for low moisture, convection is primarily the result of an island-scale sea breeze collision, whereas for higher moisture, convection can occur along the sea breeze, without the need for a collision.

## 3. Methodology

### 3.1. Cloud-resolving modelling

The model used in this study to simulate Hector is version 3.1.1 of the Weather Research and Forecast Model (WRF) model (Skamarock *et al.* 2008).

The cloud microphysics scheme used is a version of the two-moment bulk scheme by Morrison *et al.* (2005), which has been altered here to include prognostic, two-moment liquid water and rain and a new primary ice nucleation scheme (DeMott *et al.* 2010), which has been shown to vastly reduce the errors in diagnosing IN from aerosol properties. CCN activation is parameterised using the method of Twomey (1959), which has been written in a more simple form for use in the model following Rogers and Yau (1989), hence:

$$N_{CCN} = 0.88 \times C^{2/(2+k)} \times \left(70 \times w^{3/2}\right)^{(k/(2+k))} \quad (1)$$

where $N_{CCN}$ is the drop concentration (cm$^{-3}$) at cloud-base, $w$ the updraught speed in m s$^{-1}$ and $C$ (cm$^{-3}$) and $k$ are constants describing the supersaturation activity of the CCN—$N_{CCN} = Cs^k$, where $s$ is the supersaturation in percent.

Note that the model simulations presented here did not use prognostic CCN and so the processes of advection, washout and rainout and evaporation of particles forming new CCN was not represented. There are questions about the relative importance of entrained tropospheric CCN

vs CCN entrained at cloud base. Fridlind *et al.* (2004) found in simulations of thunderstorms observed during CRYSTAL-FACE that aerosols entrained between 6 and 10 km were important to the evolution of the anvil microphysics, whereas van den Heever *et al.* (2006) found a larger relative sensitivity to the aerosols entrained below 4 km. Other researchers have found the cloud properties in deep convection to be dominated by the CCN entrained at cloud base (Khain and Pokrovsky 2004). These difficulties are acknowledged although addressing these issues would require the use of high resolution, large eddy simulation (LES), that can resolve the in-cloud supersaturation and mixing at the edges of the cloud. This was not the aim of this paper and we therefore adopted the non-prognostic CCN version of the code for our simulations.

The warm rain process was parameterised using the method of Seifert and Beheng (2005), which is largely based on an analytical solution of the stochastic collection equation, with some constraints from bin microphysical modelling. No cumulus parameterisation was used in the simulations, as the model set-up should resolve the clouds in sufficient detail.

No smoothing was applied to the numerics of the dynamical core, but diffusion options for scalars were chosen to be consistent with the planetary boundary layer (PBL) physics. Positive definite advection was used for all scalars, while the defaults were used for advection of momentum.

For short-wave and long-wave radiation we used the rapid radiation transfer models (RRTM), which are new for version 3. For the surface layer and the boundary layer, the Quasi-Normal Scale Elimination method was used (again both new for version 3), while for the land surface we used the Noah land surface model, which holds temperature and moisture in 4 'soil' layers.

The runs were performed using a single domain with a horizontal resolution of 1 km and a time-step of 5 seconds, with 230 grid points in the east-west direction and 150 in the north-south direction since it was found that this configuration is optimal for simulating Hector (Zhu *et al.* 2012). This is expected to be adequate since Golding (1993) found that at least 4 km horizontal resolution was necessary to capture the general dynamics of Hector; and also that vertical resolution was important: too coarse and convection may be suppressed; hence we used 115 vertical levels, specified as 'sigma' levels. This equated to $\sim$ 50 m in the planetary boundary layer and between 100 and 400 m in the free-troposphere and the stratosphere, resulting in a model top at $\sim 23,500$ m. All runs were initialised at 18 UTC on the day prior to the case study using European Centre for Medium-range Weather Forecasting (ECMWF) reanalysis data, which were also used to provide the lateral boundary conditions through a specified outer boundary condition and nudging of the 4 adjacent outer model levels to the reanalysis data using a linear ramp. The simulations ran for 18 hours model time and were performed on quad-core PCs with multi-threading, using version 2 of the Message Passing Interface Chameleon (MPICH2) for communication between compute nodes.

### 3.2. Treatment of aerosols

Aerosol properties were measured with the UK Airborne Research and Survey Facility (ARSF) Dornier during the ACTIVE campaign, as described by Allen *et al.* (2008).

The measured aerosol properties were converted to CCN spectra by deriving the $C$ and $k$ parameters for input into the WRF model, which uses Equation 1. In order to infer CCN measurements from the data we adopted the approach of using detailed parcel model simulations with bin-microphysics, into which we input the measured aerosol size-distributions and aerosol chemical properties.

In the parcel model runs, the initial pressure, temperature and relative humidity were set equal to 950 mbar, 22°C and 99% respectively, which was consistent with air just below cloud base, and was assumed to be the same for all cases. The variations in cloud base temperature and pressure were small enough for this assumption to be valid and not affect our results. The aerosols were given their equilibrium water contents as initial conditions. We then ran the parcel model for 10 different updraught speeds ranging between 0.01 and 3 m s$^{-1}$ until after the point of CCN activation (i.e. cloud formation) and derived the number concentration of aerosols activated as CCN from the model output fields.

Our model uses the aerosol composition, size information and mixing state to derive the equilibrium vapour pressure of the particles. In the absence of information on the aerosol mixing state (i.e. internally mixed or externally mixed), we assumed all aerosols were internally mixed. Sensitivity tests performed since have shown the number of predicted CCN to be relatively insensitive to the assumption that the aerosols were internally mixed. Furthermore, assuming that the aerosol were all ammonium sulphate did not strongly affect the number of CCN either. We suspect that this is because the aerosol sizes were relatively small and so their activation is dominated by the 'Kelvin term' in the Köhler equation.

The equilibrium vapour pressure of the aerosol particles was then calculated using Köhler theory (Equation 2).

$$RH_{eq} = 100 \times \exp\left(\frac{4\sigma M_w}{RTD \times \rho_w}\right) \times a_w \qquad (2)$$

where $\sigma$ is the surface tension, $M_w$ is the molecular weight of water, $D$ is the diameter of the aerosol particle and is calculated using fits to density-mass fraction from a thermodynamic model, $\rho_w$ is the density of water, $R$ is the universal gas constant, $T$ the temperature and $a_w$ is the activity of water.

For multi-component aerosol, the activity of water for component $i$, $a_{w,i}$ is inferred from a polynomial fit to activity versus aerosol component mass-fraction data (see Equation 3) from the aerosol thermodynamic model of Topping *et al.* (2005a,b).

$$a_{w,i}(x_s) = \sum_{j=0}^{N-1} A_j x_s^j \qquad (3)$$

here, $A_j$ are the polynomial fit parameters and $x_s$ is defined as the mass-fraction of the aerosol particle—or aerosol mass divided by total mass of water and solute (see Equation 4)

$$x_s = \frac{m_s}{m_s + m_{H_2O}} \qquad (4)$$

Rearranging this, the mass of water is given by Equation 5

$$m_{H_2O} = \frac{m_s(1 - x_s)}{x_s} \qquad (5)$$

For an internal mixture of aerosol, we use the Zdanovski-Stokes-Robinson (ZSR) theory for calculating the water content. That is, the activity of water of the different components, $i$, are equal and the water content inferred from all sub components must equal the total water content. That is we solve Equation 6:

$$W - \sum_{i=1}^{M} \left( \frac{m_{s,i} [1 - x_{s,i}\{a_w\}]}{x_{s,i}\{a_w\}} \right) = 0 \qquad (6)$$

where, $W$ is the water content of the aerosol, $m_{s,i}$ is the mass of the $i^{th}$ aerosol component and the functions $x_{s,i}\{aw\}$ are the inverse of the polynomial fits (Equation 3). This equation is solved by numerical root-finding using the Z-Brent (Press *et al.* 1993) method for the values of $m_{s,i}$ that were measured (see Figure 2).

These equations are solved in size-bins in the framework of a Lagrangian parcel model for the aerosol chemical compositions and size distributions described in Figure 2 and Table I. The results of this modelling are presented in Section 4.3.

### 3.3. Data processing and analysis

The main tool for verification in this study is the C-band polarised radar, which was situated at Gunn-Point (25m ASL, Lat/Long: 12.25 S, 131.05 E). Figure 1 shows the location of the radar with respect to the Tiwi Islands and the circle shows the range of the radar.

For comparison with the model we have used the so-called 'Statistical Coverage Product', which is a time-height plot of the fraction of a defined domain that has a radar reflectivity exceeding a certain threshold (see May *et al.* 2009, for details).

While the model does not hold reflectivity as a prognostic variable, one can use the microphysical fields to calculate what the radar reflectivity factor should be and convert this to the decibel scale. We did this calculation (using a similar methodology to Swann 1998) so that it was completely consistent with the assumed size distributions within the model microphysics scheme. This method was preferred over converting the observed reflectivity and polarisation fields to microphysical classifications to avoid errors that may occur during the retrieval. However, it is recognised that that this method also assumes no attenuation of the beam and that Rayleigh scattering applies. The wavelength of this radar is $\sim 5$ cm, which is large enough so that Rayleigh scattering can be assumed valid; however, although the effect of attenuation slightly alters the values of the coverage product, this is effect is not large enough to affect the outcomes of the paper.

The domain used to calculate the statistical coverage product is shown as the rectangle in Figure 1. Threshold values of reflectivity that we have chosen to compute the product were: (i) reflectivity values larger than 10 dBZ and (ii) reflectivity values larger than 40 dBZ (although later it was found that 30 dBZ provided a fairer comparison in some of the cases). The 10 dBZ threshold allows one to compare the spatial distribution of precipitation, including regions of light rain and other precipitation, while the 40 dBZ threshold refers to the spatial distribution of the regions of high (or convective) precipitation only.

In order to provide an objective method for evaluating the simulations the corresponding statistical coverage
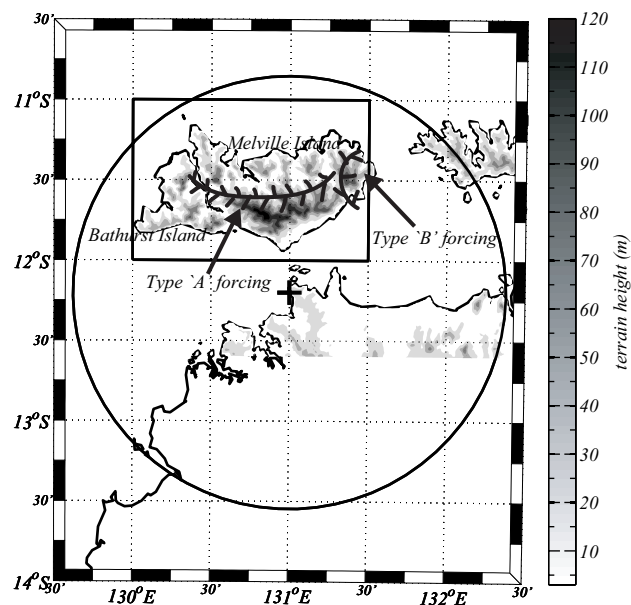


**Figure 1.** The domains used to generate radar and satellite statistics. The range of the radar is shown by the circle centered at approximately $12°15'S$, $131°E$. Also note that the rectangular domain defined to encompass the Tiwi Islands was not fully covered by the radar due to restrictions on its range. Also shown is the terrain height in metres and typical convergence lines that form over the islands (see text).

products, which were derived from the WRF model fields were analysed using a metric called the fractions skill-score, $FSS$, which has been used previously for rainfall verification over different scales (Roberts and Lean 2008).

The fractions skill score, $FSS$, is given as:

$$FSS = 1 - \frac{FBS}{\frac{1}{N}\left(\sum_{j=1}^{N} p_j^2 + \sum_{j=1}^{N} o_j^2\right)} \qquad (7)$$

$$FBS = \frac{1}{N}\sum_{j=1}^{N} (p_j - o_j)^2 \qquad (8)$$

where $N$ is the total number of grid points, $p_j$ is the modelled value at grid point $j$, $o_j$ is the observed value at grid point $j$. $FSS$ is equal to unity for a perfect match between model ouput and observational data and equal to zero for a simulation that has no agreement with the data. In order for the comparison between model ouput and observational data to be consistent in scale we applied a 3-grid averaging filter in the horizontal (to average model reflectivity up to the 3 km horizontal resolution radar grid) and a 2-grid averaging filter in the vertical (to average the vertical resolution to 500 m in accord with the radar grid). The results of this model verification are the main subject of this study and are presented in Section 4.7.

## 4. Results

### 4.1. Aerosol chemical composition

As described by Allen *et al.* (2008) the aerosol chemistry changed throughout the ACTIVE period due to the changing meteorology. At the start of the campaign in November, during the transition from the dry to the wet season the land over the Tiwi Islands was routinely burned by land managers to reduce the risk of uncontrolled bush fires. This resulted in the predominant aerosol chemical composition

being organic. In fact, even into December, when the biomass burning was much reduced the organic signal was still strong with organics comprising between 58% and 83% of the total sub-micron volatile mass loading, as measured with an Aerosol Mass Spectrometer (AMS)—Figure 2(a,b and c). As Figure 2(a,b and c) shows the remainder of the aerosol mass was measured to be ammonium sulphate, and to a lesser extent sulphuric acid. Ammonium nitrate comprised very little of the aerosol mass loading throughout the whole experiment.

In January, during the active monsoon, there was widespread cloud and more oceanic convection. The widespread cloud and precipitation served to remove the 'high' aerosol loadings by wash out and rain out processes, leaving only the ammonium sulphate sources to replenish the aerosol; hence, throughout the monsoon period, ammonium sulphate had the highest mass loading (between 74 and 44%—Figure 2(d,e)). Following the monsoon there was a break period where the wind direction returned to easterly; during this time the dominant aerosol chemical composition changed back to organic (Figure 2(f)).

Note that throughout all periods black carbon aerosol was measured to be a very small fraction of the total aerosol mass loading (see Figure 7 of Allen *et al.* 2008), and sea salt comprised a small number fraction of the total aerosol; therefore, the aerosol compositions shown in Figure 2 are thought to be representative for the periods considered.

### 4.2.   Aerosol size distributions

Aerosol size distributions in the inflow to Hector, and in the monsoon regime, were measured with: an Ultra High Sensitivity Aerosol Spectrometer (UHSAS) by Droplet Measurement Technologies (DMT); an Aerosol Spectrometer Probe (ASP-100) by DMT; a GRIMM optical particle counter (Model 1.109, GRIMM Germany); and an Forward Scattering Spectrometer Probe (FSSP) by DMT. As described by Allen *et al.* (2008) concentrations were high during the biomass burning period, following which concentrations reduced throughout December. During the monsoon regime the concentrations reduced to very low values (due to wash out and rain out) after which, in the break period, there was a slight increase in the total measured concentration.

In order to provide input size distributions for bin microphysical modelling (Section 4.3) we were able to fit tri-lognomal mode aerosol size-distributions to the measured size distributions where a single lognormal mode is described by Equation 9.

$$\frac{dN}{dD} = \frac{N_L}{D\sqrt{2\pi}\log(\sigma_g)} \exp\left(\frac{\log\left(\frac{D}{\bar{D}}\right)^2}{\log(\sigma_g)^2}\right) \quad (9)$$

here, $N_L$ is the total number, $D$ is the aerosol diameter, $\bar{D}$ is the median diameter and $\log(\sigma_g)$ is the natural logarithm of the standard deviation of the distribution. The fit parameters for these modes are shown in Table I, where it can be seen that the concentrations in each mode were generally high throughout November and early December; reduced slightly throughout December; greatly reduced throughout January (due to the monsoon); and slightly increased over January values throughout February.

Also shown in the final column of Table I is an estimate of the mean number concentration of aerosol particles that had

diameters larger than $0.5\mu$m, $n_{aer,0.5}$. This was calculated from the data as it is an input to the primary ice nucleation scheme (DeMott *et al.* 2010) so has been calculated for each day. The scheme calculates the number of active primary ice nuclei, $n_{IN,T_k}$, given the number concentration of aerosols larger than $0.5\mu$m and the ambient temperature. DeMott *et al.*'s parameterisation is:

$$n_{IN,T_k} = a\,(273.16 - T_k)^b\,(n_{aer,0.5})^{c(273.16-T_k)+d} \quad (10)$$

where $a = 0.0000594$, $b = 3.33$, $c = 0.0264$, $d = 0.0033$, $T_k$ is the temperature in Kelvin, $n_{aer,0.5}$ is the number density (number per milli gram of air) of aerosol particles with diameter greater than $0.5\mu$m and $n_{IN,T_k}$ is the ice nuclei number density (number per gram of air). In fact the calculated values of $n_{IN,T_k}$ show little sensitivity to the measured $n_{aer,0.5}$ in Table I so there was little variation in the concentrations of assumed IN between cases. Note that in DeMott *et al.*'s parameterisation the number of aerosol particles greater than $0.5\,\mu$m should be considered as a proxy for the number of IN. This does not mean that only the particles greater than $0.5\,\mu$m are IN.

The tri-lognormal fits to the aerosol presented in Table I may be used by other researchers wanting to perform aerosol-cloud studies for the ACTIVE observational period.

### 4.3.   Cloud condensation nuclei and ice nuclei

Here we show the results of the application of a cloud parcel model to derive CCN spectra for input into WRF from the measured aerosol chemical composition and size distribution information.

The parcel model simulations described in Section 3.2 were performed for each day listed in Table I. This produced a total of 10 simulations for each day (i.e. 10 values of vertical wind) for 15 case studies on different days: a grand total of 150 simulations, which each provided one value of $N_{CCN}$ and $w$.

We then grouped the paired data of $N_{CCN}$ and $w$ by meteorological and compositional period (i.e. burning, pre-monsoon, break) and fitted Equation 1 to those data, using non-linear regression, thus deriving the $C$ and $k$ parameters for each meteorological period. The grouped data and fitted curves plus the curve fits and fit parameters are shown in Figure 3. These fit parameters are also shown in Table II, as well as the mean number concentration of aerosols larger than $0.5\mu$m (last column) for the days within those distinct periods (see Table I). It can be seen that curves of $N_{CCN}$ vs $w$ are stratified into roughly three regimes, which we will refer to as 'high' aerosol; 'medium' aerosol and 'low' aerosol. These three regimes form the basic sensitivities to be investigated with the WRF model.

A hypothesis to be tested is therefore that: *using the observationally-constrained aerosol input in the WRF model simulations of Hector gives the best agreement to the observations*. The rest of the paper will now focus on addressing this hypothesis.

### 4.4.   Overview of Hector storm development

Results from 7 Hector cases are reported in this paper, the dates of which are in Table III. Clearly this is too many cases to present in detail, but in order to understand some of the important Dent aerosol effects influencing the development of
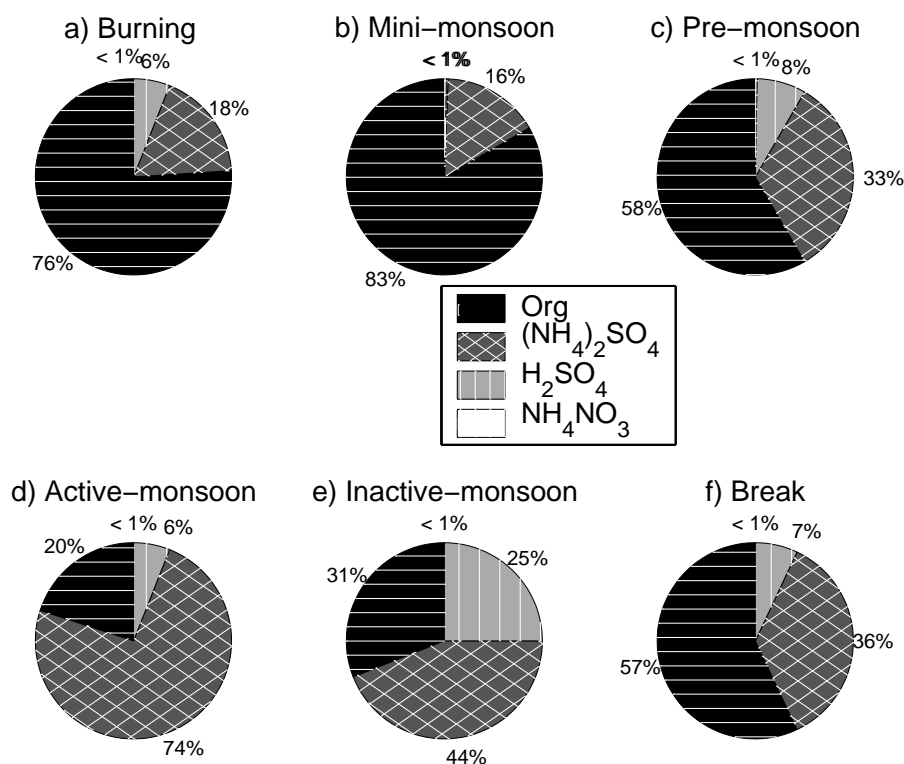
**Figure 2.** Uses data from an aerosol mass spectrometer and performs a charge balance to infer an approximate composition of the aerosol. Please note we are not able to say what the actual organic material was. From the information available in the mass spectrum we justified the use of levoglucosan as the representative compound, but noted that the results were fairly insensitive to this assumption. Note this is different to the plot in Allen *et al.* (2008), which showed percentage mass of ions, rather than compounds.

Table I. Triple log-normal fits to the measured aerosol size distributions. Fits are valid in the range $0.055 \leq D \leq 1.0 \mu m$. Also shown in the last column are the number concentrations of particles larger than $0.5 \mu m$.

| | First mode | | | Second mode | | | Third mode | | | IN (L$^{-1}$) |
|---|---|---|---|---|---|---|---|---|---|---|
| Date | $N_L$ (cm$^{-3}$) | log $(\sigma_g)$ | $D_m$ ($\mu$m) | $N_L$ (cm$^{-3}$) | log $(\sigma_g)$ | $D_m$ ($\mu$m) | $N_L$ (cm$^{-3}$) | log $(\sigma_g)$ | $D_m$ ($\mu$m) | |
| | | | | Burning period | | | | | | |
| 2005-11-15 | 4.6134e+04 | 7.96946e-01 | 9.855e-03 | 1.1203e+03 | 3.75414e-01 | 1.381e-01 | 5.9303e-01 | 2.41030e-01 | 7.066e-01 | 881 |
| 2005-11-16 | 7.7420e+04 | 7.79752e-01 | 8.171e-03 | 1.1612e+03 | 3.98469e-01 | 1.253e-01 | 3.1803e+00 | 6.89010e-01 | 4.507e-01 | 652 |
| 2005-11-19 | 9.0578e+03 | 3.14692e-01 | 3.047e-02 | 6.0113e+02 | 4.09782e-01 | 1.101e-01 | 2.2404e+00 | 8.38339e-01 | 2.600e-01 | 537 |
| 2005-11-28 | 4.9976e+03 | 3.46958e-01 | 2.939e-02 | 7.7432e+02 | 4.33152e-01 | 1.169e-01 | 3.6667e+00 | 7.07375e-01 | 2.963e-01 | 1120 |
| 2005-12-01 | 3.9087e+04 | 4.89427e-01 | 1.492e-02 | 7.1533e+02 | 3.90142e-01 | 1.151e-01 | 1.4161e+00 | 6.42094e-01 | 4.596e-01 | 671 |
| | | | | Pre-monsoon | | | | | | |
| 2005-12-04 | 7.7867e+04 | 5.73510e-01 | 1.073e-02 | 4.9045e+02 | 3.76761e-01 | 1.224e-01 | 7.3422e-01 | 4.23935e-01 | 5.390e-01 | 450 |
| 2005-12-05 | 7.9875e+04 | 6.06900e-01 | 1.006e-02 | 4.2579e+02 | 3.92167e-01 | 1.328e-01 | 2.0420e-01 | 2.05085e-01 | 7.346e-01 | 341 |
| | | | | Active-monsoon | | | | | | |
| 2006-01-19 | 4.3977e+04 | 2.66045e-01 | 2.261e-02 | 6.4980e+02 | 7.70975e-01 | 4.718e-02 | 1.4321e-01 | 2.01205e-01 | 9.525e-01 | 839 |
| 2006-01-20 | 7.3365e+04 | 5.42089e-01 | 1.001e-02 | 3.6316e+02 | 4.96578e-01 | 9.283e-02 | 1.1662e-01 | 2.18976e-01 | 7.114e-01 | 230 |
| | | | | Inactive-monsoon | | | | | | |
| 2006-01-25 | 2.5881e+02 | 5.45670e-01 | 6.250e-02 | 4.3629e+00 | 4.54311e-01 | 2.500e-01 | 1.2709e-01 | 2.43218e-01 | 1.000e+00 | 411 |
| | | | | Break period | | | | | | |
| 2006-02-06 | 3.0080e+02 | 4.42380e-01 | 7.826e-02 | 1.4359e+01 | 5.84943e-01 | 1.352e-01 | 3.3864e-01 | 8.99999e-01 | 6.492e-01 | 383 |
| 2006-02-08 | 1.0882e+03 | 3.48881e-01 | 2.854e-02 | 1.8857e+02 | 4.50541e-01 | 9.859e-02 | 6.8633e-01 | 8.11019e-01 | 2.600e-01 | 168 |
| 2006-02-09 | 7.7578e+04 | 6.48332e-01 | 6.924e-03 | 2.9930e+02 | 4.28966e-01 | 1.130e-01 | 1.4382e+00 | 3.02207e-01 | 6.828e-01 | 195 |
| 2006-02-10 | 1.1327e+04 | 7.86972e-01 | 8.803e-03 | 2.2923e+02 | 4.29147e-01 | 1.078e-01 | 4.0268e-01 | 7.46427e-01 | 4.304e-01 | 205 |
| 2006-02-14 | 7.8538e+04 | 7.73678e-01 | 5.052e-03 | 2.9153e+02 | 4.07732e-01 | 1.178e-01 | 1.6621e-01 | 2.86165e-01 | 6.661e-01 | 191 |

Table II. Parcel model derived fits to C and k and number of aerosol $> 0.5 \mu m$

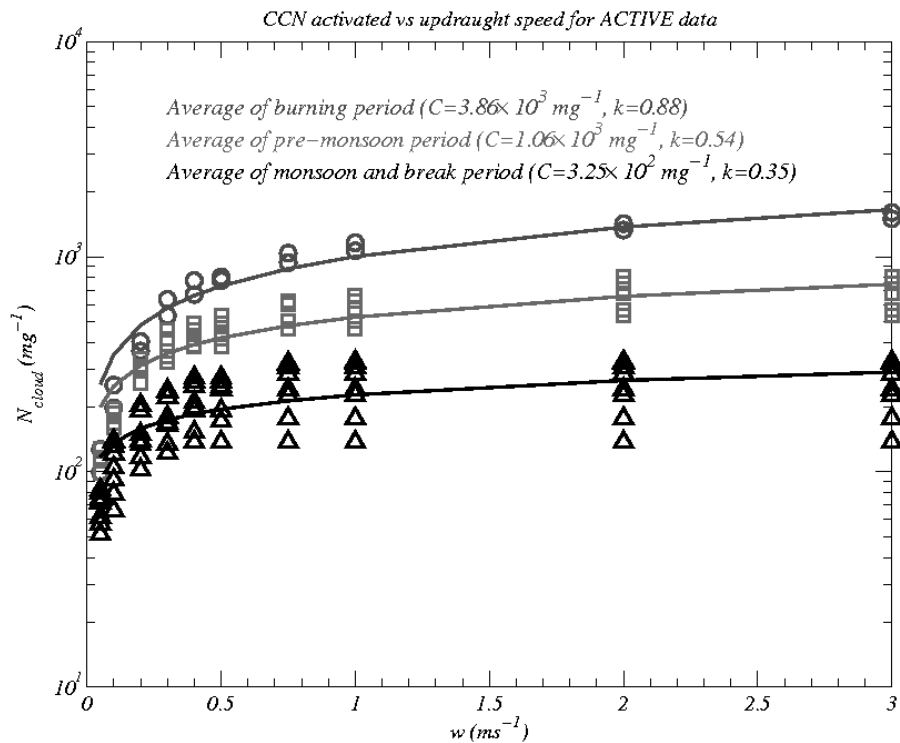| Period | C (mg$^{-1}$) | k | $n_{>0.5 \mu m}$ (L$^{-1}$) |
|---|---|---|---|
| Burning period (2005-11-15 and 2005-11-16) | 3860 | 0.88 | $\sim 772$ |
| Pre-monsoon (2005-11-19 to 2005-12-05) | 1060 | 0.54 | $\sim 396$ |
| Monsoon and break (2006-01-19 to 2006-02-14) | 325 | 0.35 | $\sim 328$ |

**Figure 3.** Model derivation of the CCN properties showing the number of CCN activated vs updraught speed

Hector we have chosen to focus on presenting more detail from three of the cases, observed in 'high', 'medium' and 'low' aerosol environments (as described in Section 4.3). Respectively, these cases are the 01-Dec-2005, 06-Dec-2005 and 06-Feb-2005 Hectors.

Figure 4 shows radar reflectivity plots for the three main cases mentioned above. For the 01-Dec-2005 case the location of the main cell was over Melville Island, with a weaker cell situated over Bathurst Island (Figure 4a). The height of the detraining region on this day was approximately between 8 and 15 km (Figure 4b).

Similar plots for the 06-Dec-2005 case are shown in Figures 4c and d. Here smaller cells of convection were situated on the ridge that is present on the islands (Figure 4c see also Fig. 1). The height of the convective turrets reached $\sim 17$ km (Figure 4d) and later the anvil cirrus rapidly advected to the west (not shown).

The 06-Feb-2006 case was a weaker storm, which formed over Melville Island on the sea breeze (Figure 4e). The height of this storm was lower than the previous two cases, with the detraining region occuring between 8 and 14 km (Figure 4f).

In order to get more of a picture of the time sequence of Hector development we show the modelled outgoing longwave radiation (OLR) for each of the three cases discussed above. The OLR shows the location of clouds as white areas in Figure 5.

Figure 5 shows a time sequence of the modelled OLR for the 01-Dec-2005, 06-Dec-2005 and the 06-Feb-2006 cases. The general pattern for these cases is for a convergence to occur in an east-west line over the islands (see Figures 5a, b and c, which show the initial stages of convection for each case). In both the 01-Dec-2005 and 06-Dec-2005 cases, the initial stages of the convection are influenced by the shallow ridge over Melville Island (Figures 5a, b). This

is less so for the 06-Feb-2006 case (Figure 5c) due to the humidity distribution; however, a realistic sea-breeze circulation was captured by the model. As was the case for the observations the 01-Dec-2005 case shows two main cells (Figure 5d), while the convection in the 06-Dec-2005 is more distributed.

The anvil cirrus that is generated in the 01-Dec-2005 case spreads out more or less evenly in all directions (Figure 5d), which is due to low wind speed aloft for this case. In the 06-Dec-2005 the anvil cirrus is transported westward (Figure 5e). Both the 01 and 06-Dec-2005 cases produced an extensive anvil region (Figure 5g, h), while the weaker 06-Feb-2006 case produced an anvil of lower spatial extent.

For comparison with the model, Figure 6 shows the equivalent OLR calculated from the Multi-functional Transport SATellite (MTSAT) channel 1 brightness temperature. Whilst the agreement between model and data is not exact, it is clear that the model does a reasonable job of capturing the development of Hector. Evidence of this for the 01-Dec-2005 case is shown by the convergence on the north-east coast of the Tiwi Islands (Figures 5 and 6a) and the development of two convective cells for this case (Figures 5 and 6d). Additionally for the 06-Dec-2005 case the development of a single cell, with an anvil that moves westward is consistent between both model and observations (Figures 5 and 6b, e and h). Furthermore, for the 06-Feb-2006 case some convergence toward the north of the Islands, which then results in a cell developing towards the west of the Islands shows satisfactory agreement between model and data (Figures 5 and 6c,f and i).

### 4.5. Summary of the sensitivities

In this study we ran WRF for 10 different case studies that occurred throughout the two observational periods for each
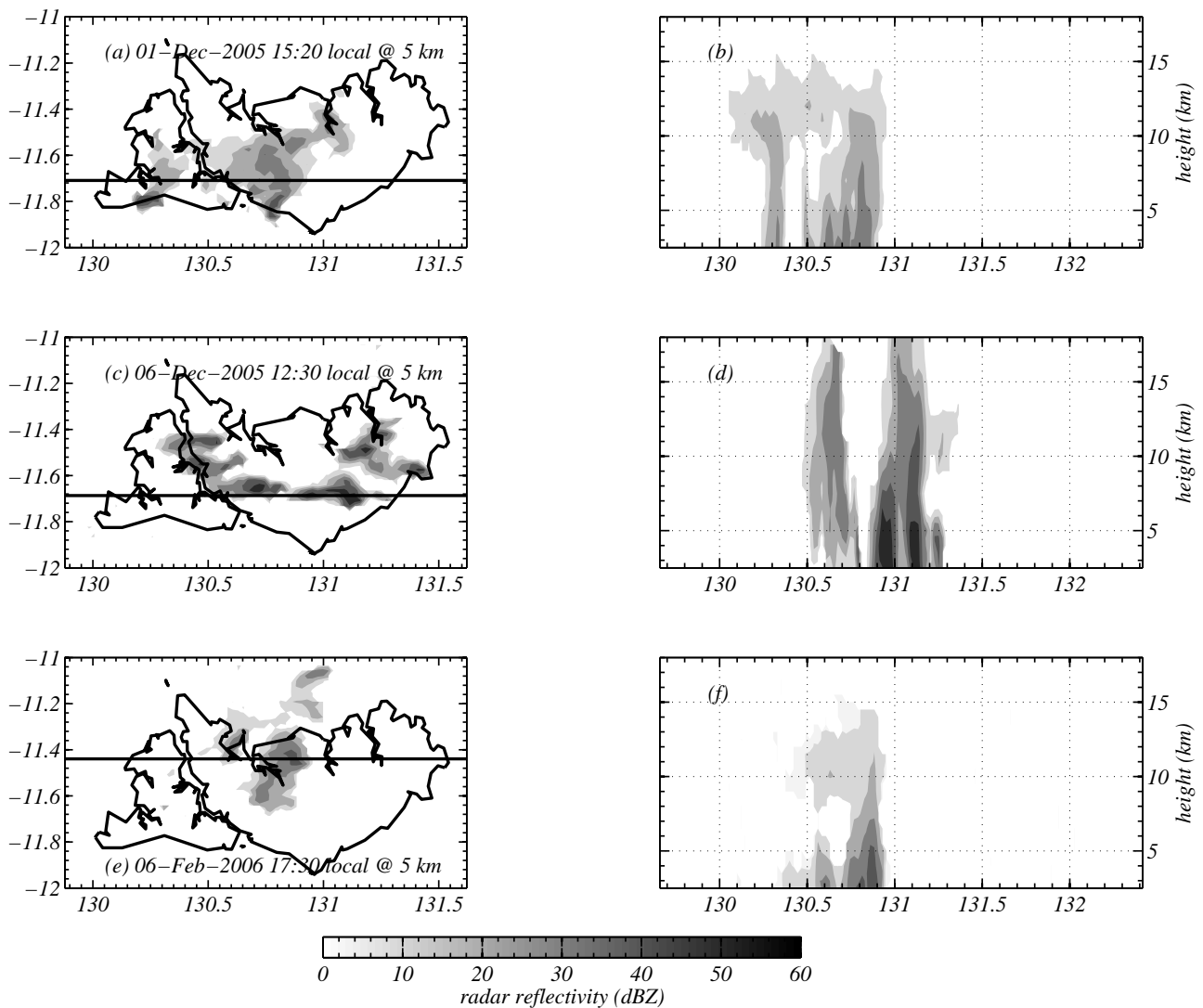
**Figure 4.** A summary plot of the radar observations for three cases presented in this paper. (a, b) show the observed reflectivity at 5 km altitude and a vertical scan against longitude along the black line in (a) respectivity for the 01-Dec-2005 case; (c, d) show the same but for the 06-Dec-2005 case; and (e, f) show the same but for the 06-Feb-2006 case.

of the different aerosol inputs described in Table II ('High'; 'Medium' and 'Low'). This resulted in a grand total of 30 WRF simulations. Some of the cases failed to reproduce the observations as in reality the Hectors on those days were affected by storms advecting into the model domain, so were not well captured by our single domain simulations; hence we will not report on those simulations here. This leaves 7 cases on which the remainder of the paper will focus, the dates of which are in Table III.

Rather than describe all the sensitivities for each case we have opted to focus on just two days, which summarise well the sensitivities to aerosol for the different Hector cases. While these are different to the storm cases discussed in Sections 4.5 and 4.6, they are chosen because they aid our discussion of the range of sensitivities to aerosol that occurred within the modelled cases.

Figure 7 shows percentiles of time-series data from the simulations for the 16th November 2005 Hector. These were produced by computing domain averaged values for OLR and accumulated precipitation and outputting the maximum value of the vertical velocity at each time level to generate time-series data. Percentiles of the time-series data were taken over the time period 12:30 to 20:30 (local time) as this represented the period where the convection was most active. Shown in the Figure are model predictions of the out-going long-wave radiation, the maximum vertical wind and the domain averaged accumulated precipitation. The median value of OLR has a variation of $\sim 4$ W m$^{-2}$ between the different aerosol loadings with OLR generally increasing with decreasing aerosol loading. This is because (not shown in the figures herein): (i) the cirrus produced by the storms with lower aerosol input are generally lower and warmer, thus having a higher black-body temperature and; (ii) they are thinner and do not trap as much long-wave radiation as the case with 'high' aerosols. There is also a slight increase in the median updraught speed as aerosols are reduced. However, for 'high' aerosols there are more brief episodes of very high updraught speeds, as seen by the high value of $W_{max}$ at the 87.5th percentile in the Figure. In this case, interestingly, precipitation is highest when aerosols are high and the median values vary by approximately 20%, which is the opposite of what would be expected in shallower clouds (i.e. the warm rain process is usually stronger when aerosol concentrations are low).
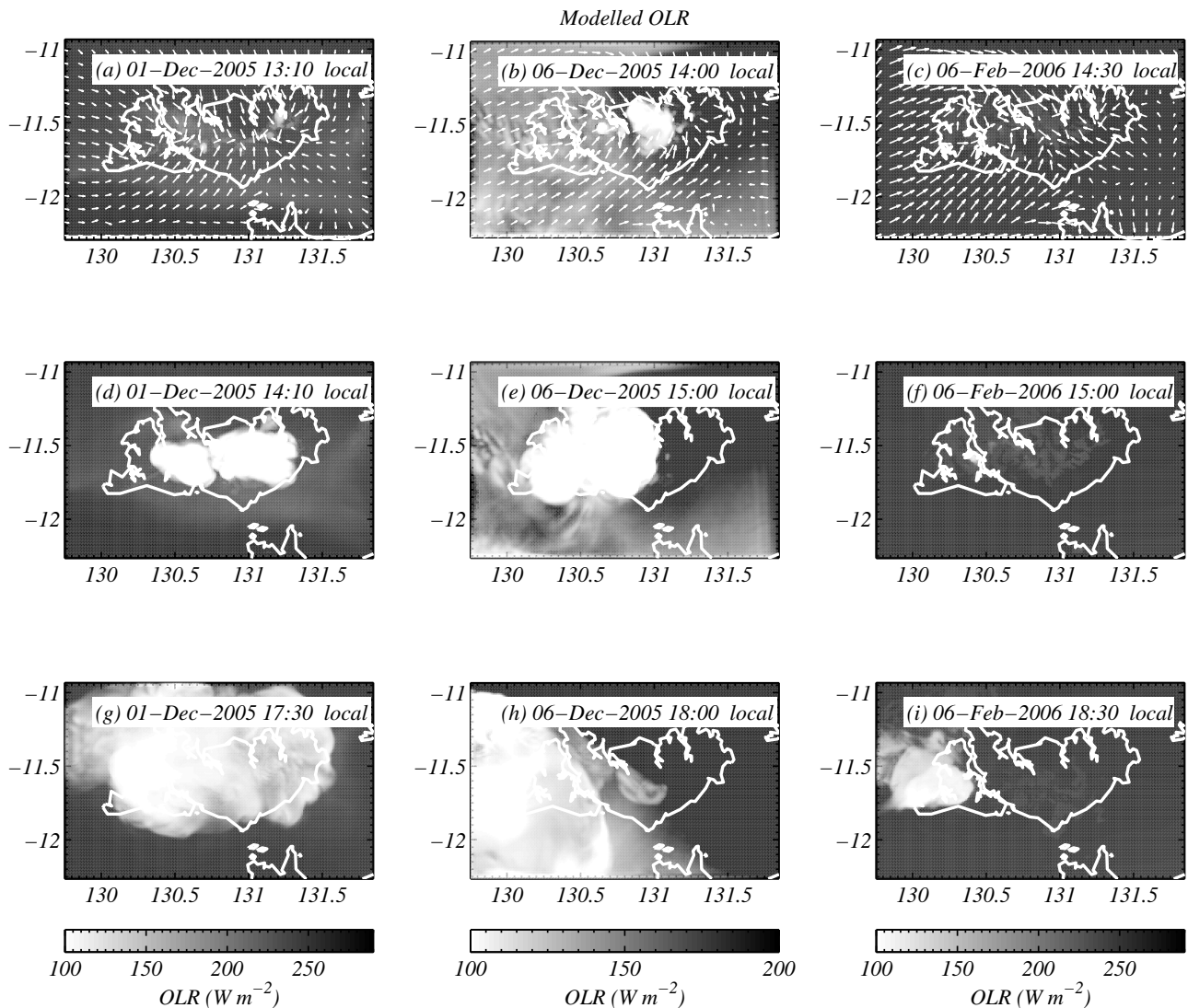
*Modelled OLR*



**Figure 5.** A summary of the development of OLR for three modelled Hector cases (01-Dec-2005; 06-Dec-2005 and 06-Feb-2006). a, d and e show the time sequence for the 01-Dec-2005 case at 13:10, 14:10 and 17:30 local time; b, e and h show the development for the 06-Dec-2005 case at 14:00, 15:00 and 18:00 local time; and c, f and i show the development for the 06-Feb-2006 case at 14:30, 15:00 and 18:30 local time.

The seemingly counter-intuitive finding of 'low' aerosols producing less precipitation and a thinner anvil is because during this meteorological period the mid-troposphere was relatively dry (May *et al.* 2009), causing a significant fraction of the detraining precipitation to evaporate before it reached the surface (this has been discussed by Khain *et al.* 2005, and others). It has been shown through numerical modelling of thunderstorms that in some situtuations less evaporation will occur in cases of 'high' aerosols than 'low' aerosols (Khain *et al.* 2005), which may explain why the 'high' aerosol case has increased precipitation. Hence, the 'high' aerosol cases precipitate more because less evaporation occurs in the mid-troposphere. It is worth noting that in both pre and post-Christmas periods, soundings are reasonably similar to the GATE-261 sounding on which the maritime simulations of Khain *et al.* (2005) were based.

The same plots for the simulations of the 3rd December 2005 Hector are shown in Figure 8. Again the 'low' and 'medium' aerosol simulations produce a marginally thinner anvil region than the 'high' aerosol simulation (refer to the

median OLR—left panel) and again OLR varies by around a few W m$^{-2}$. However, in this case precipitation on the ground increases with decreasing aerosols with a variation in median precipitation $\sim 10\%$. The mid-level humidity in this case was higher than in the 16th November case and this probably contributed to the opposite sensitivity in the model, but also it appeared that part of the reason was due to the way in which the gust-fronts from neighbouring cells interacted with each other (as discussed by Tao *et al.* 2007; van den Heever and Cotton 2007). This is a rather random effect and may completely change the modelled sensitivities of the storm to aerosols, depending on where exactly the convective cells formed on a particular day.

The exact locations of the gust fronts may either enhance or suppress the storm considerably. We note that this non-linear effect does not agree with the results of Khain *et al.* (2005), who found that increased concentrations of aerosols resulted in more intense storms for two soundings. There are two main differences here: (i) we have simulated more cases than the Khain *et al.* study, so it is likely we will see more variation in the responses to aerosol; and (ii) we note
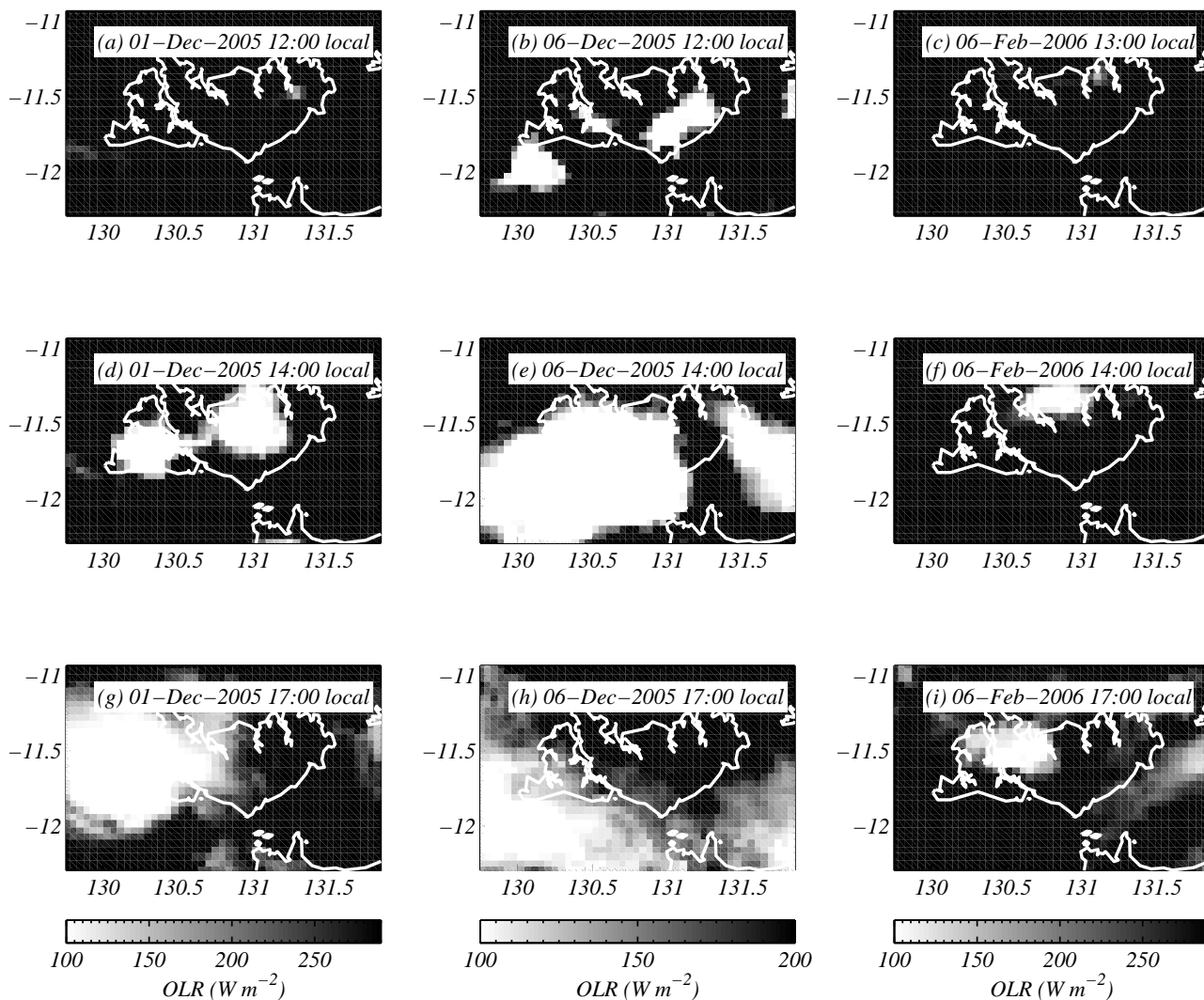
**Figure 6.** A summary of the development of OLR for three observed Hector cases (01-Dec-2005; 06-Dec-2005 and 06-Feb-2006). a, d and e show the time sequence for the 01-Dec-2005 case at 12:00, 14:00 and 17:00 local time; b, e and h show the development for the 06-Dec-2005 case at 12:00, 14:00 and 17:00 local time; and c, f and i show the development for the 06-Feb-2006 case at 13:00, 14:00 and 17:00 local time.
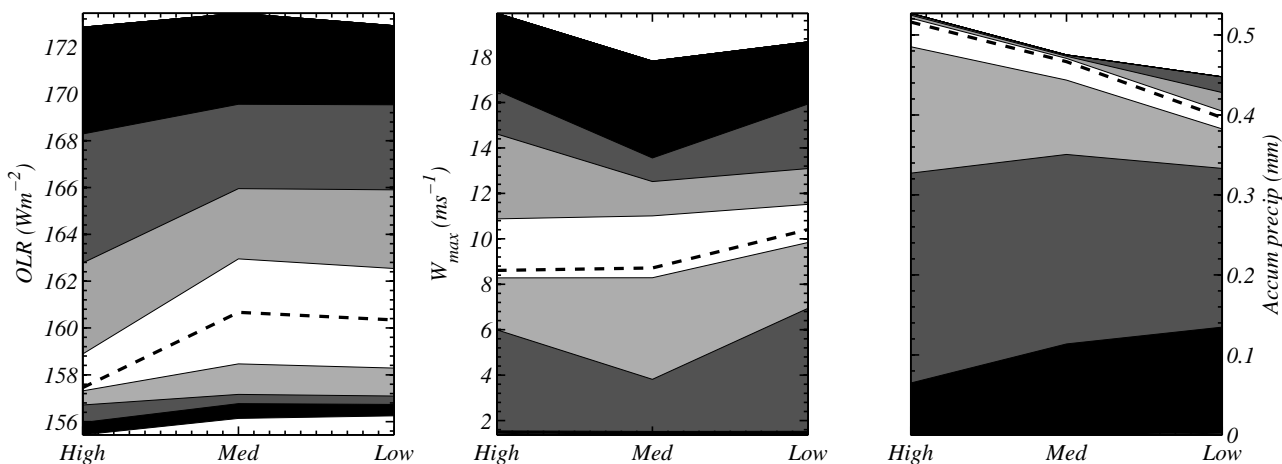


**Figure 7.** Summary plots showing how aerosols effect the outgoing longwave radiation (left); maximum updraught speed (middle); total domain averaged precipitation (right) for the 16-Nov-2005 case. The plots represent a period in time over which the storm was active and the anvil was present ∼8 hours, with the dashed line representing median values and the white contour representing the 43.75 and 56.25th perctile and each subsequent level of gray scale representing a further plus or minus 12.5 percentiles. Values at the top boundary thus represent the 87.5th percentile and values at the bottom represent the 12.5th percentile. The x-axis is the different level of aerosol loading: 'High', 'Medium' or 'Low' (see Table II).

that the Khain *et al.* study used a two-dimensional model and hence the lower dimensionality may produce less of a random effect of the modelled gust fronts on the strength of the storm.

As for the previous case, the median of the maximum updraught speed shows a general trend to increase with decreasing aerosols, but in this case there are episodes of high updraughts for 'medium' aerosol loadings.

In summary the effect of aerosols typically changed the OLR by a few W m$^{-2}$ and could either increase or decrease precipitation on the ground depending on the dryness of the mid-troposphere or the complex interactions between neighbouring cells. No simple relations between aerosols and the properties of the simulated clouds could be found. Table III shows a summary of the range in median values for all cases reported in this paper; the effect of aerosols on OLR is a few W m$^{-2}$ and the effect they have on precipitation on the ground is $\sim 20\%$, which is sufficiently large to be considered an important aerosol indirect effect. Table III also indicates the direction of the trend with increasing CCN concentrations. Broadly speaking it is shown that increasing aerosol reduces OLR and reduces precipitation, although there are exceptions to this. The effect of CCN concentration on median updraft velocities is less clear cut, with some cases showing a positive trend and some negative.

### 4.6.   Storm radar statistics: observed and modelled

Here we show observed and modelled reflectivity time-height and time-longitude plots to illustrate how aerosol loadings affect intense Hector thunderstorms.

Whilst the simulations do not reproduce the observations in their entirety, it is shown that better skill scores are possible if we initialise with the observed CCN; hence, they are sufficiently accurate to discern aerosol effects on the precipitation properties of the storms. In some cases the WRF model predicted the convection to occur slightly later than the observations, perhaps by $\sim 1$ hour, and also predicted it to occur in a slightly different location; hence , as discussed later, to enable a fair comparison we slightly shifted the modelled statistical coverage plots in time and in longitude for a few of the cases.

Figure 9 shows both observed and modelled time-height statistical coverage plots of the fraction of the domain in Figure 1 that has a radar reflectivity larger than 10 dBZ for the 01-Dec-2005 Hector case. Figure 9(a) is for that observed by the radar, (b) is for the model simulation with 'high' aerosol; (c) for 'medium' aerosol and (d) for 'low' aerosol. This Hector case was actually observed to have 'High' aerosol concentrations entering the in-flow of the storm. The coverage products with 'medium' and 'low' aerosol tend to produce cells that are separated in time, as noted by the region of coverage at about 1800 hours local time. This is not evident in the observations (Figure 9a), nor is it evident in the simulation with 'high' aerosol (Figure 9b). We note that the simulated anvil is not as extensive as the observed anvil (region of high coverage between 8 and 14 km); however, the 'high' aerosol simulation gives the most long lasting anvil, giving encouraging qualitative agreement between the model and observations.

Figure 10 shows a time-longitude, Hovmoller-type plot for the statistical coverage of the fraction of the domain that has a radar reflectivity larger than 10 dBZ, evaluated at a constant altitude of 5km, for the 1-Dec-2005 Hector case study. We chose 5 km as it is high enough so that artefacts such as ground clutter and beam distortion do not affect the results. As for the time-height plots it is shown that 'medium' and 'low' aerosols (Figure 10c,d) tend to produce cells that are more separated in time, whereas the observations and the 'high' aerosol case (Figure 10a,b) produce a much more continuous feature in the time-longitude coordinates (for example there is no clear gap between the cells at $\sim$ 1600 hours local and at 130.75 E). We interpret this as the cell initiating at $\sim$ 131.2 E as precipitating early in the 'medium' and 'low' aerosol simulations, whereas in the 'high' aerosol simulation it does not. Gust-front dynamics also play a role in changing the path of both cells. The strong precipitation in the 'medium' and 'low' aerosol cases from the cell at $\sim$ 131.2 E gives rise to cold pools that result in the secondary cells reaching higher altitudes in these model cases (analysed, but not shown), whereas in the 'high' aerosol case, weaker precipitation from the cell at $\sim$ 131.2 E results in weaker cold pool forcing and the secondary cells being weaker.

Figure 11 shows the same time-height plots as Figure 9, but for the 6-Dec-2005 Hector case. This case was observed to have medium aerosol concentrations. It can be seen that the observed storm (Figure 11a) had relatively low coverage early on in the day at around 1000 local time; furthermore, the anvil region was quite extensive having $\sim 30$ % coverage of the domain between 8 and 13 km at around 1400 local time. The low radar coverage at $\sim 1000$ local time is not present for the 'High' aerosol simulation (Figure 11b) and the fraction of the domain covered by the anvil is relatively low for both the 'high' and 'low' aerosol cases (Figure 9b,d). Only the 'medium' aerosol simulation has both the early low-level radar coverage and high anvil coverage (Figure 11c), although admittedly the anvil is not as persistent as the observations (the possible reasons for this are discussed in Section 5).

Figure 12 shows the same time-longitude, Hovmoller-type plots as Figure 10 but for the 6-Dec-2005 Hector case study. The observations (Figure 12a) show a region of low coverage to the west at approximately 1200 local time and no coverage to the east at approximately 1600-1700 local time. Neither of the model runs simulate the early cumulus congestus particularly well. It should be noted that the aerosol measurements used to initialise the model on this day were predominantly made to the east of the islands so a gradient in the aerosol concentrations over the islands may affect the formation of congestus. This effect is not explored in the present paper. The main Hector initiated to the east and travelled west before dissipating over the sea. In the 'high' aerosol simulation (Figure 12b) there is no region of low radar coverage to the west at 1200 local time, but there is a region of low radar coverage to the east at 1500-1600 local time (which is not present in the observations). Similar coverage is also present for the 'low' aerosol case (Figure 12d). There is lower radar coverage in the same position for the 'medium' aerosol case, which also has some coverage present to the west at $\sim 1200$ local time. Admittedly the coverage is too small when compared to the observations, and there are potential issues in the gradient of aerosol properties over the islands—for instance the 'low' aerosol simulation seems to give the best representation for the west side of the islands. On balance though, two points lead us to the suggestion that the 'medium aerosol case is the best representation of reality. These are (i) that the 'medium

Copyright © 2011 Royal Meteorological Society

*Prepared using qjrms4.cls*

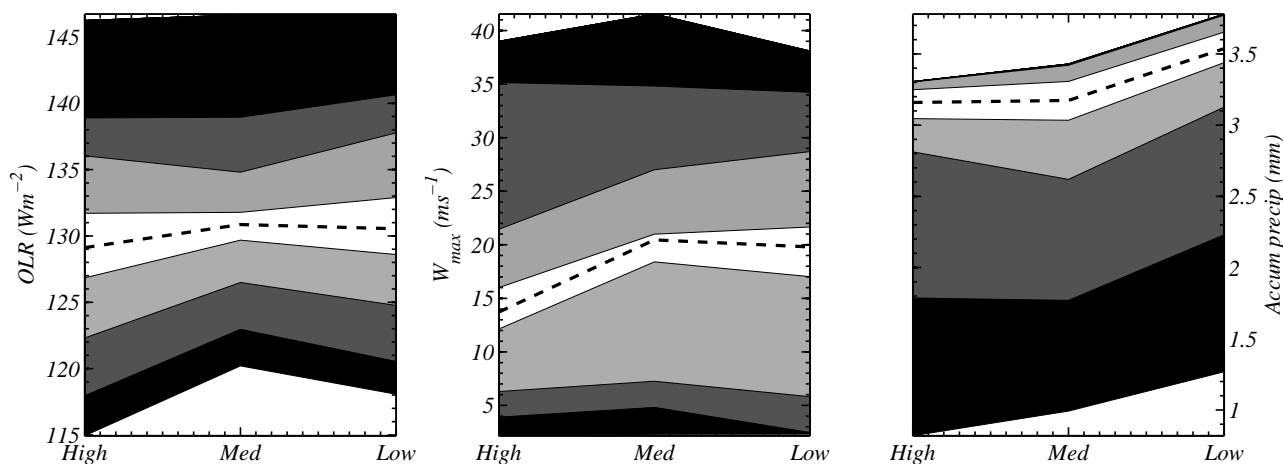*Q. J. R. Meteorol. Soc.* **00**: 1–20 (2011)

**Figure 8.** As Figure 7 but for the 03-Dec-2005 case

Table III. A summary of the range in median values of OLR, updraught speed and accumulated precipitation (expressed as a percent of the precipitation in the sensitivity that had the highest precipitation) for all cases. Also shown is whether the trend is positive (+) or negative (−) with increasing aerosol.

| Case study | Range in median OLR (W m$^{-2}$) | Range in median $W_{max}$ (m s$^{-1}$) | Range in median precip. (%) |
|---|---|---|---|
| 2005-11-16 | 3.2(−) | 1.80(−) | 23% (+) |
| 2005-12-01 | 7.1(−) | 8.07(−) | 9% (−) |
| 2005-12-03 | 1.7(−) | 6.74(−) | 10% (−) |
| 2005-12-06 | 0.3(+) | 3.00(+) | 24% (−) |
| 2006-02-06 | 0.7(−) | 0.63(−) | 22% (−) |
| 2006-02-08 | 0.2(−) | 1.44(+) | 41% (−) |
| 2006-02-10 | 3.4(−) | 1.86(−) | 5% (−) |

aerosol case has a high anvil extent, which is closer to the observations than the other two cases and (ii) the on-set of precipitation lower down in the cloud is closer to the observations in the 'medium and 'low aerosol cases than the 'high aerosol case.

Figure 13 shows the same time-height plots as Figure 9, but for the 6-Feb-2006 Hector case. This case was observed to have low aerosol concentrations. Two or three cells are visible in the observations (Figure 13a), which were broadly reproduced in all of the simulations, regardless of aerosol input. However, in the 'high' aerosol case (Figure 13b) it is noticeable that the first cell has larger coverage than the secondary cells. This was not so for the 'medium' aerosol case, where the first cell has less coverage (Figure 13c). The first cell also has slightly less areal coverage in the 'low' aerosol case (Figure 13d), which is consistent with the observations. Another feature worth noting is that in the observations, the first significant radar coverage is seen at ∼ 1130 local time whereas in the 'high' aerosol case it is seen at ∼ 1230 local time. Both the 'medium' and 'low' aerosol cases are more consistent with the observations in this respect, and the main reason for this was attributed to faster warm rain production in the two lower aerosol model cases. It should be noted that for this case study the production of the first echo was delayed by approximately 40 minutes for this case, so all runs were shifted in time by 40 minutes to compare with the observations; this time shift is small enough so that the main forcing mechanisms (e.g. radiation, boundary conditions) should not alter too much so the delay in precipitation may be attributed to model spin-up.

To summarise the results of this section we we argue that better agreement between observations and model are obtained when CCN loadings consistent with the *in-situ* aerosol observations are used. The simulations suggest that there are microphysical effects occurring within the clouds that have a significant effect on the dynamics of the Hector storms, by altering the locations where latent heat is being released and by removing condensate by precipitation processes—e.g. they alter cloud-top heights and the position of cells. Altering the position of the convective cells relative to one another can result in non-linear effects on storm strength by the interaction between gust-fronts and other circulations (e.g. Tao and Simpson 1984).

### 4.7. Fractions skill score analysis

By visual comparison of the statistical coverage product we identified several features of the storms that seem to depend on aerosol concentrations and composition. To perform this comparison objectively we now examine the fractions skill score (using Equation 7) for each case study to see if using the measured aerosol concentration and composition improves the skill of the simulations. We have done this for both the time-height and the time-longitude statistical coverage products at several different threshold levels of reflectivity, but present only two threshold values here for brevity.

#### 4.7.1. Total coverage of precipitation

Here we show the calculations of the fractions skill scores for different assumed aerosol loadings for threshold values
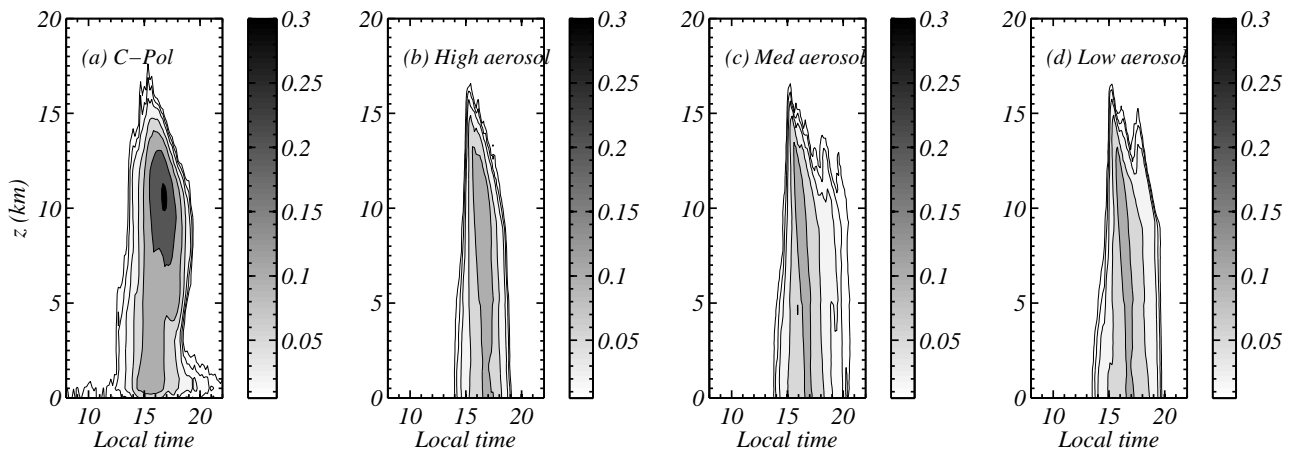
**Figure 9.** Statistical coverage product as a time-height map of the fraction of the domain in Figure 1 covered by radar echoes larger than or equal to 10 dBZ. This is for the 1-Dec-2005 Hector case. (a) is that observed by the radar; (b) is that simulated with 'high' aerosol input; (c) is that simulated with 'Medium' aerosol input; (d) is that simulated with 'Low' aerosol input. Note on this day we observed aerosol consistent with 'High' aerosol input.
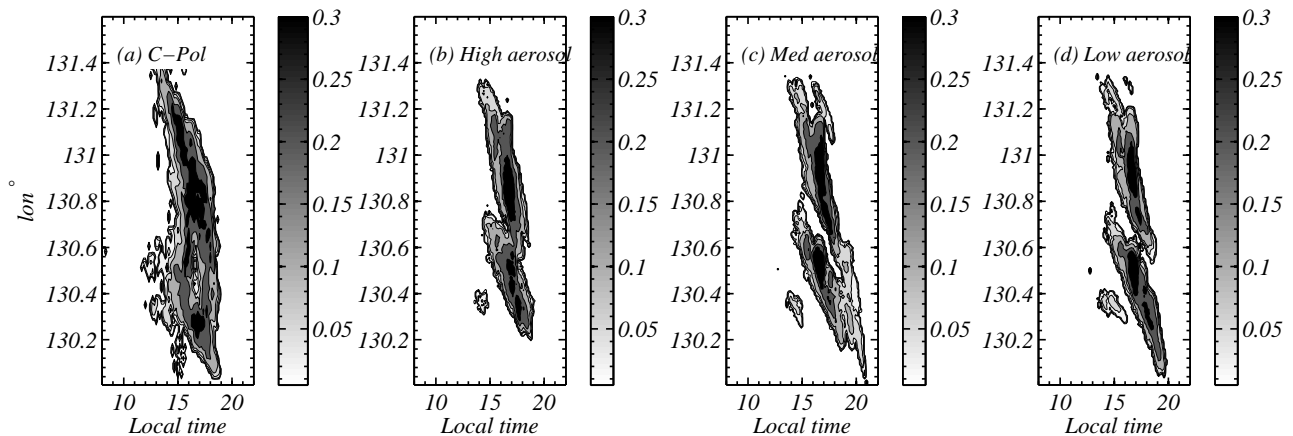


**Figure 10.** Fraction of grid points along all values of latitude in the domain (Figure 1), which are above a threshold reflectivity of 10 dBZ at the value of longitude shown (y-axis). The plots are constructed for a height of 5 km, for the 1-Dec-2005 Hector case, panels as in Figure 9

of reflectivity larger than 10 dBZ. This relatively low value of reflectivity represents the coverage of light rain, or other precipitating particles (e.g. snow).

Figure 14 shows the fractions skill scores for both the time-height plots (e.g. Figure 9) and the longitude-height plots (e.g. Figure 10). Both the 16-Nov-2005 and the 01-Dec-2005 Hector cases had 'high' aerosol and it is clear that the fractions skill score is highest when observationally-constrained CCN is used in the model for both the time-height score and the time-longitude score (Figure 14a,b—left two clusters of bars).

The 03-Dec-2005 and the 06-Dec-2005 cases had 'medium' aerosol input and it is shown that the time-longitude plot has the highest fractions skill score for 'medium' aerosol for both cases; however, for the time-height plot this is only true for the 6-Dec-2005 case and 'high' aerosols give the best score for the 3-Dec-2005 case (Figure 14a,b—3rd and 4th clusters of bars).

The 06-Feb-2006, 08-Feb-2006 and the 10-Feb-2006 all had 'low' aerosol inputs and Figure 14a,b shows—3 right most clusters of bars—that 'low' aerosols gave the best fractions skill scores.

In summary all cases except perhaps that of the 3-Dec-2005 are better simulated when observationally-constrained aerosol is used as input. For the 3-Dec-2005 case the difference between scores in the time-height plots is small and the spatial coverage in the time-longitude plot is better when observationally-constrained aerosol are used.

### 4.7.2. *Coverage of strongest precipitation*

To evaluate how well the model reproduces the regions of strong convective precipitation we calculated the fractions skill scores for different assumed aerosol loadings for threshold values of reflectivity larger than 40 dBZ for the time-height scores and larger than 30 dBZ for the time-longitude score. We have used a different value for the time-longitude scores since when we inspected the scores for a 40 dBZ threshold the results appeared to have a somewhat random ordering with respect to aerosol loadings. On closer inspection this was because of slight variations in the spatial positions of the strongest cells in the model. On balance we believe that choosing a lower threshold was valid for the time-longitude plot as it removed this problem.

Figure 15 shows the fractions skill scores for both the time-height plots (e.g. Figure 11) and the longitude-height
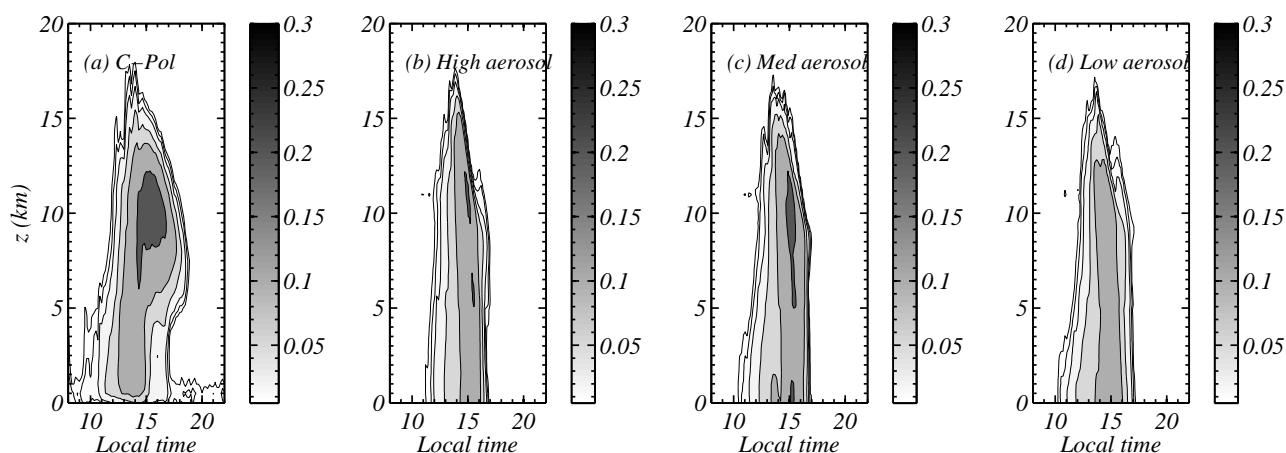
**Figure 11.** Same as Figure 9 but for the 6-Dec-2005 Hector case where we observed 'Med' aerosol
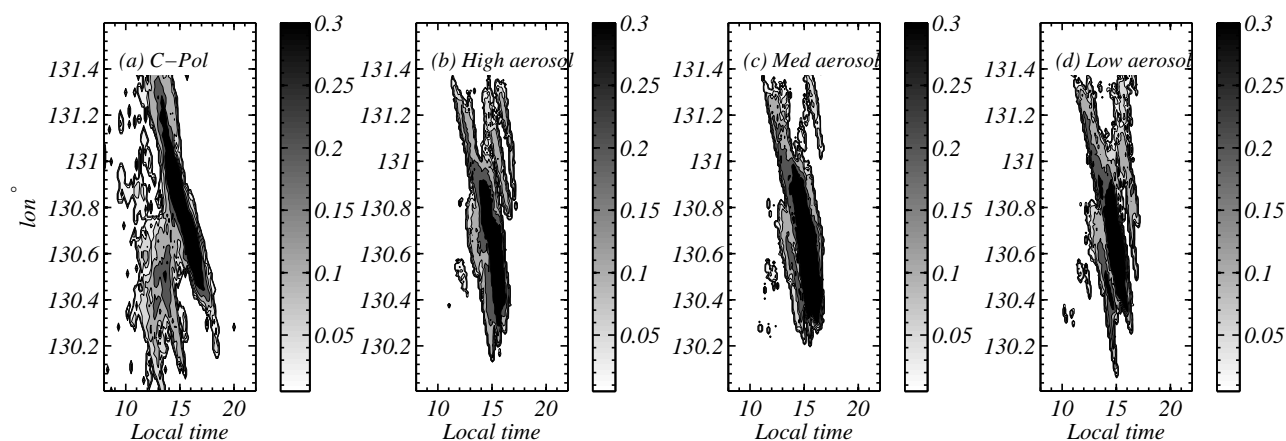


**Figure 12.** Same as Figure 10 but for the 6-Dec-2005 Hector case where we observed 'Med' aerosol

plots (e.g. Figure 12). As above the 16-Nov-2005 and the 01-Dec-2005 Hector cases had 'high' aerosol and it is clearly shown that the fractions skill score is highest when observationally-constrained CCN are used in the model for both the time-height score and the time-longitude score (Figure 15a,b—left two clusters of bars).

The 03-Dec-2005 and the 06-Dec-2005 cases both had 'medium' aerosol input. Only in one case however—03-Dec-2005—does the time-longitude plot show the highest fractions skill score for 'medium' aerosol. Similarly, the time-height scores, with 'medium' aerosol gave the highest score for the 06-Dec-2005 case, but 'high' aerosol was best for the 03-Dec-2005 case (Figure 15a,b—3rd and 4th clusters of bars).

Despite the uncertainties in defining the CCN concentration and in calculating model reflectivity, we are encouraged to find that the model is best able to simulate the observations in most cases when the proper CCN concentration is specified. However it may be that the aerosol input used in the model is not exactly the same as the conditions on the day for either case, and that the model is sensitive to small variations in aerosol input: recall when we derived the CCN concentrations for each case we averaged the data together to produce only three CCN spectra, 'high', 'medium' and 'low' (Figure 3) and aerosol on the day could

be somewhere in between these. However, there may be other reasons for the discrepancy. It is noted that these plots are only evaluating the strongest areas of convection, and slight differences between observations and modelling on the exact location and timing of the convection may have adversely affected the fractions skill score for these two cases.

The 06-Feb-2006, 08-Feb-2006 and the 10-Feb-2006 all had 'low' aerosol inputs and indeed 'low' aerosols gave the best fractions skill scores (Figure 15a,b, 3 right most clusters of bars).

In summary, we argue that both the 'high' aerosol cases and the 'low' aerosol cases have higher fractions skill scores when observationally-constrained aerosol are used in the model. For the 'medium' aerosol cases this is not so clear, but may be due to errors in the radar reflectivity calculation, or slight differences between the model input aerosol and the actual aerosol observed on the day.

## 5. Discussion

While it was not explored explicitly in this paper we can infer that using ECMWF reanalysis data to initialise the model, and to drive its boundary conditions, is superior to using operational ECMWF analyses, since the study by Zhu *et al.* (2012), which used operational analyses, found
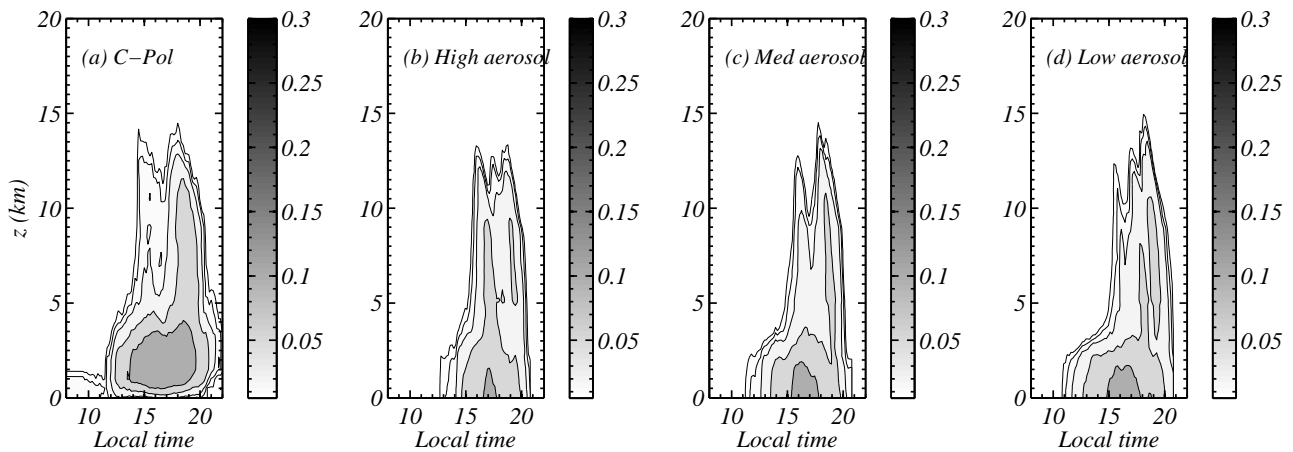
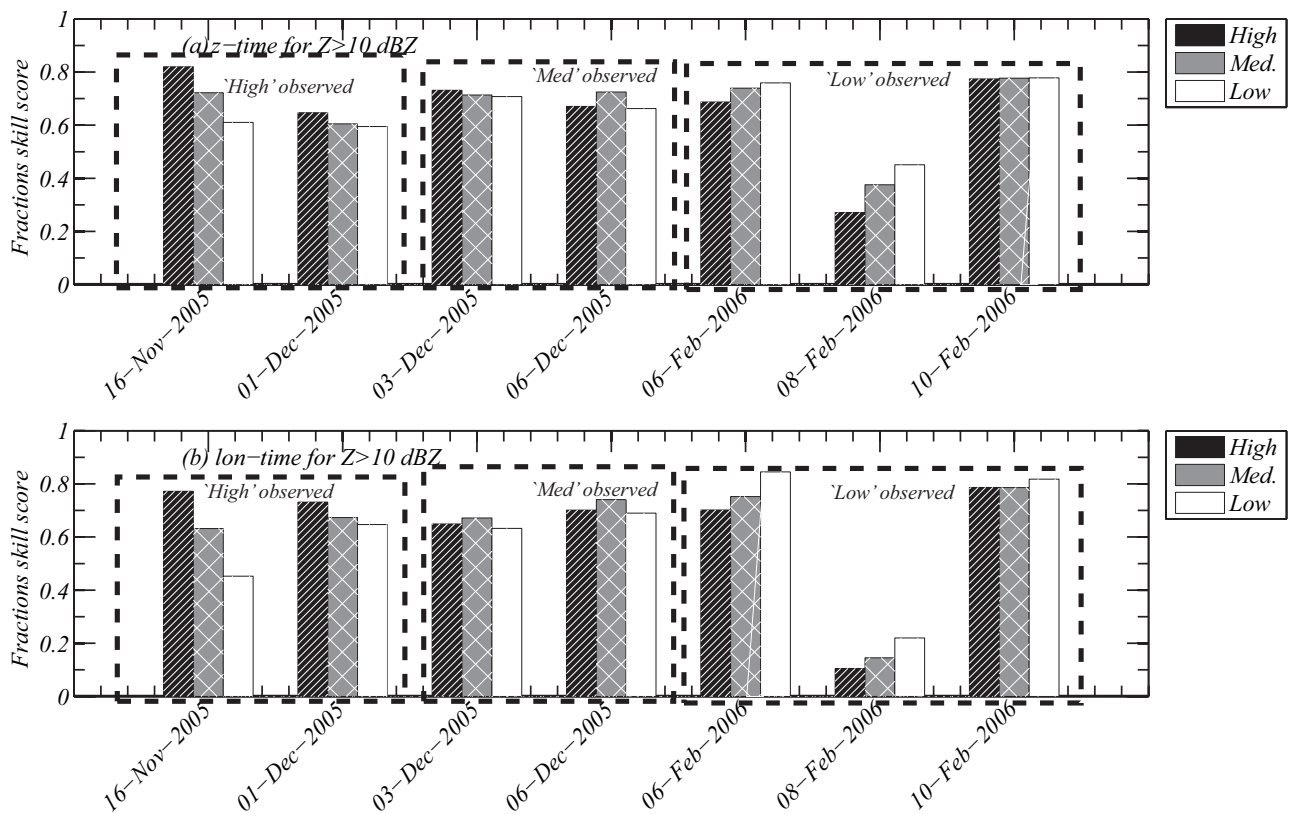**Figure 13.** Same as Figure 9 but for the 6-Feb-2006 Hector case where we observed 'Low' aerosol



**Figure 14.** (a) shows the fractions skill score for the time-height plots of the fraction of the domain in Figure 1 that have reflectivity larger than 10 dBZ. The fraction skill score is calculated over the whole time period of the model simulation for all altitudes; (b) shows the fractions skill score for the longitude-height plots of the fraction of the domain at 5 km that has reflectivity larger than 10 dBZ.

far poorer agreement between observations and model results than that reported here, where reanalysis datasets were used.

This combined modelling and observational approach provides evidence that aerosols can affect the cloud coverage for deep tropical convection and that the double-moment microphysical scheme used in this study was broadly capable of simulating the aerosol effects provided realistic aerosol inputs are used.

May *et al.* (2009) analysed radar, thermodynamic profiles and aerosol data from the same project and found

some association with aerosols effecting properties of the convection. For instance they found that lower aerosol concentrations produced wider rain coverage than the storms observed in the 'high' aerosol period and vice-versa, but this could not be decoupled from the effects of the thermodynamic and wind profiles. In their study it was pointed out that as well as the pre-Christmas period having higher aerosol concentrations than the post-Christmas period, the earlier period also had a drier mid-level troposphere, which could have evaporated the precipitation-sized particles during their descent.
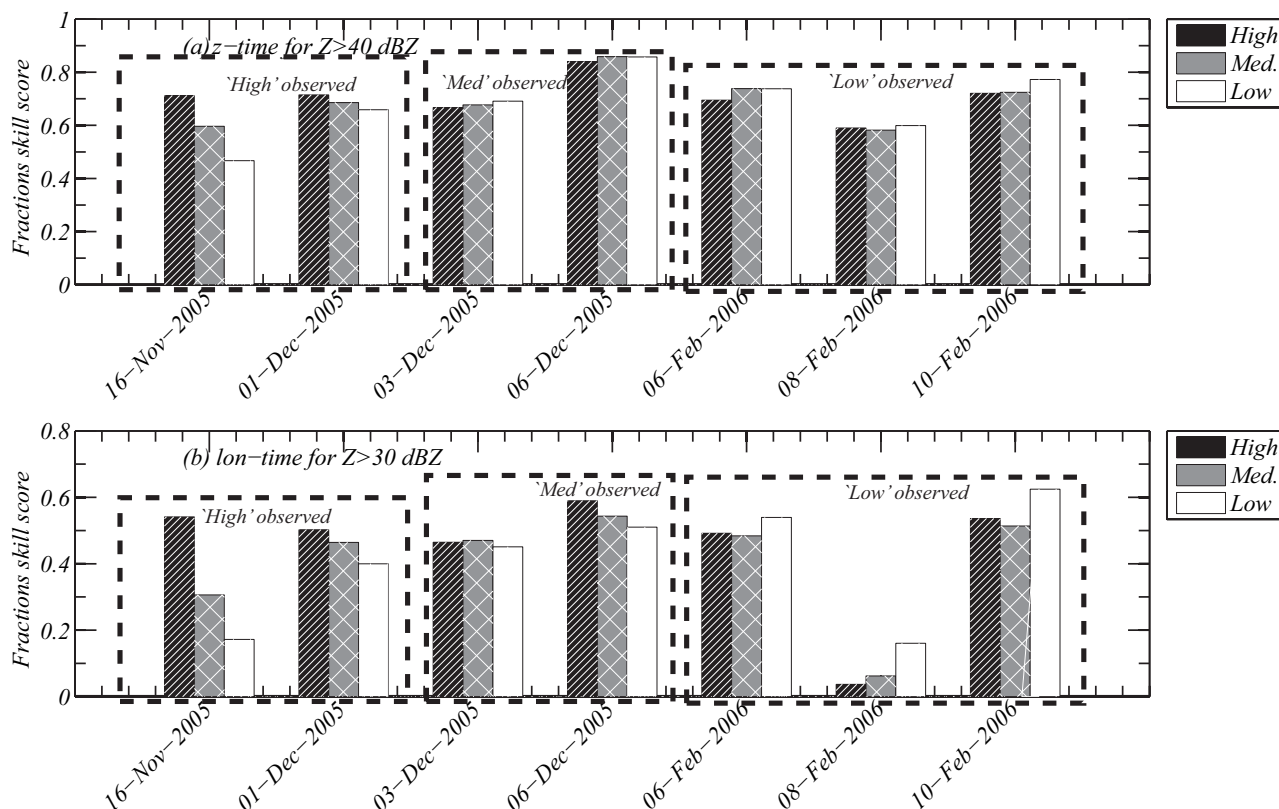
Copyright © 2011 Royal Meteorological Society

*Prepared using qjrms4.cls*

*Q. J. R. Meteorol. Soc.* **00**: 1–20 (2011)

**Figure 15.** (a) shows the same as Figure 14a, but for a threshold reflectivity of 40 dBZ, which represents strong convective precipitation; (b) shows the same as Figure 14b but for a threshold reflectivity of 30 dBZ. Note that for the longitude-time plots we trialled a threshold reflectivity of 40 dBZ, but the results appeared rather random, which is because of slight variations in the exact position of the strong convective cells between model and observation.

The study has provided evidence that aerosols may have indeed affected the properties of the deep convection during the ACTIVE campaign. But rather than affect the convection in a general way, the effect of aerosols on the storm properties seems to be case-dependent, with meteorology playing a large role in the way the clouds respond to aerosol. For instance, in some cases higher aerosols give increased precipitation on the ground, but the reverse can also occur. Aside from the more obvious effects of CAPE and CIn on the strength of convection (May *et al.* 2009) aerosols, as a result of their effects on modifying precipitation, influence the locations and the collisions between gust fronts, which themselves play a role in either enhancing or suppressing the convection, an effect that has been noted in 2-d simulations of convection by Tao *et al.* (2007). It is also noted that wind shear also influences the effects of aerosols in 2-D cloud-resolving-model (CRM) simulations (Fan *et al.* 2009).

Results from satellite studies have proliferated hypotheses on how and why convective clouds respond to aerosols (e.g. Koren *et al.* 2008; Rosenfeld and Woodley 2001; Rosenfeld 1999). We find no evidence for a simple relationship between aerosols and convective intensity (see Figures 7 and 8); however, we concede that the range of CCN concentrations observed during ACTIVE were not as large as may be observed in other regions and more robust relationships may be found when CCN concentrations are much higher than the highest observed during ACTIVE.

As noted in Section 4.6 the anvil region in the model simulations tended to be less persistent than was observed.

The reasons for this could be due to the use of an ice-aggregation efficiency, $E_{agg}$, of 0.1 being used at all temperatures in the Morrison *et al.* (2005) microphysics scheme. Recent results Gallagher *et al.* (2012) show that the anvil region of Hector from the ACTIVE campaign— same campaign as reported here—and may have large ice-ice aggregation efficiencies, as large as $\sim 0.5$ or higher. Since an aggregation efficiency of 0.1 appears to be too low at these temperatures one might expect that the modelled crystals do not grow large enough and result in the lower modelled reflectivities in the anvil region.

Another factor that influences anvil extent and persistence in the model is that the assumed density of snow in the Morrison *et al.* microphysics scheme may be too high at these high altitudes. The default density of snow in the Morrison *et al.* scheme is set to $100\,\mathrm{kg\,m^{-3}}$, which is rather high. It is likely that this high-density snow precipitates too rapidly in the model, resulting in a less persistent anvil. Images taken in the outflow of the storm by the Egrett aircraft show that many of the ice particles form in chains (see Figure 16), which have a much lower bulk density than $100\,\mathrm{kg\,m^{-3}}$. These linear chains probably result from high electric fields within the storms, which cause the crystals to align in this way (Connolly *et al.* 2005). Further work is needed to evaluate if either of these factors change the persistence of the modelled anvil region to better match the data.
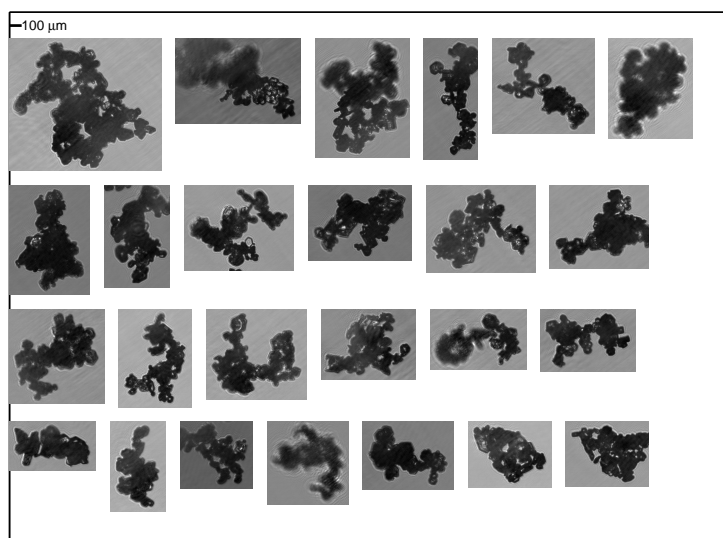
**Figure 16.** Images of chain-aggregates of ice crystals taken with a CPI during a research flight in the cirrus outflow region of Hector. Note the fact that the aggregates form in linear chains of monomers, which are sometimes folded. These crystals likely have a lower bulk density than is currently used in the model.

## 6. Conclusions

This paper has shown that taking into account aerosol properties can result in better skill scores for model simulations of the Hector thunderstorm. This is especially true for cases when aerosol concentrations are 'high' and when they are 'low' in the context of this study. 'Medium' aerosol simulations are *mostly* improved when aerosols are taken into account, although this is less clear than for the extremes in aerosol loading.

The conclusions drawn from the study are:

- Including aerosol effects in island forced convective cases can improve the simulation with regard to radar reflectivity distributions versus height and the equivalent spatial distributions.
- The aerosol effects are non-linear and depend on how neighbouring convective cells interact with each other. Sometimes the trend was for increasing aerosol to produce more precipitation and vice-versa. This is in contrast to what has been reported previously for 2-D simulations (Khain *et al.* 2005), where high aerosol concentrations were shown to invigorate secondary clouds, but similar to what has been reported for 3-D simulations (van den Heever and Cotton 2007).
- The aerosol indirect effects may produce significant local radiative effects, which are of the order of several watts per square metre over the course of a day, and much higher over shorter time scales. To address the climatological importance of these effects would require much longer integrations over larger domains.
- The aerosol effects on precipitation on the ground were of the order of 10-20% and arise because of microphysical effects within the cloud and the feedback they have on the storm dynamics. We note that Khain *et al.* (2008) have discussed the fact that 2-d simulations may overestimate the aerosol effects due to overestimating the recirculation in convective clouds.

The results have implications for satellite remote sensing studies of the aerosol effects on clouds as meteorology is shown to cause the aerosol effects to be non-linear and case dependent, due to the intricacies of the thermodynamic profile and the interactions between gust-fronts. One caveat is that the range in CCN concentrations investigated here is rather small when compared to other studies and more robust relationships may be found when exploring such a wide range in CCN concentrations. This raises the question of whether general relationships might be present in other parts of the world having higher aerosol concentrations, such as the Amazon basin.

Although the aerosol effects were significant on the local scale, it should be borne in mind that on the larger scale these effects may be much lower. Using 2-d simulations van den Heever *et al.* (2011) found that for a domain size of ∼10,000 km the total impact of aerosols may be lower due to shallow clouds compensating against aerosol indirect effects associated with congestus and deep convection.

# References

Allen G, Vaughan G, Bower KN, Gallagher MW, Williams PI, Flynn MJ, Hamilton J, Crosier J, Connolly PJ, Coe H, Choularton TW, Allan JD, Lewis A. 2008. Aerosol and trace-gas measurements in the darwin area during the wet season. *J. Geophy. Res.* **113**(D06306).

Allen G, Vaughan G, Brunner D, May PT, Heyes W, Minnis P, Ayers JK. 2009. Modulation of tropical convection by breaking rossby waves. *Quart. J. Roy. Met. Soc.* **135**(Part A): 125–137.

Carbone R, Wilson J, Keenan T, Hacker J. 2000. Tropical island convection in the absence of significant topography. part i: Life cycle of diurnally forced convection. *Mon. Wea. Rev.* **128**: 3459–3480.

Connolly PJ, Choularton TW, Gallagher MW, Bower KN, Flynn MJ, Whiteway J. 2007. Cloud resolving simulations of intense tropical, hector thunderstorms: Implications for aerosol cloud interactions. *Quart. J. Roy. Met. Soc.* **132**: 3079–3106.

Connolly PJ, Saunders CPR, Gallagher MW, Bower KN, Flynn MJ, Choularton TW, Whiteway J, Lawson P. 2005. Aircraft observations of the influence of electric fields on the aggregation of ice crystals. *Quart. J. Roy. Met. Soc.* **131**: 1695–1712.

Crook A. 2001. Understanding hector: The dynamics of island thunderstorms. *Mon. Wea. Rev.* **129**: 1550–1563.

DeMott PJ, Prenni AJ, Liu X, Kreidenweis SM, Petters MD, Twohy CH, Richardson MS, Eidhammer T, Rogers DC. 2010. Predicting global atmospheric ice nuclei distributions and their impacts on climate. *Proc. Nat. Acad. Sci.* **107**: 11 217–11 222.

Ekman AML, Engström A, Wang C. 2007. The effect of aerosol composition and concentration on the development and anvil properties of a continental deep convective cloud. *Quart. J. Roy. Met. Soc.* **133**: 1439–1452.

Fan J, Yuan T, Comstock JM, Ghan SJ, Khain A, Leung LR, Li Z, Martins JV, Ovchinnikov M. 2009. Dominant role by vertical wind shear in regulating aerosol effects on deep convective clouds. *J. Geophy. Res.* **114**(D22206): doi:10.1029/2009JD012 352.

Fridlind AM, Ackermann TP, Jensen E J, Heymsfield AJ, Poellot MR, Stevens DE, Wang D, Miloshevich LM, Baumgardner D, Lawson P, Wilson JC, Flagan RC, Seinfeld JH, Jonsson HH, Vanreken T, Varutbangkul V, Rissman TA. 2004. Evidence of the predominance of mid-tropospheric aerosols as subtropical anvil cloud nuclei. *Science* **304**: 718–722.

Gallagher MW, Connolly PJ, Crawford I, Heymsfield AJ, Bower KN, Choularton TW, Allen G, Flynn MJ, Vaughan G, Hacker J. 2012. Observations and modelling of microphysical variability, aggregation and sedimentation in tropical storm cirrus outflow regions. *Atmos. Chem. and Phys.* **in press**.

Golding BW. 1993. A numerical investigation of tropical island thunderstorms. *Mon. Wea. Rev.* **121**: 1417–1433.

Keenan T, Morton BR, Manton MJ, Holland G. 1989. The island thunderstorm experiment (itex)–a study of tropical thunderstorms in the maritime continent. *Bull. Amer. Met. Soc.* **70**(2): 152–159.

Khain A, BenMoshe N, Pokrovsky A. 2008. Factors determining the impact of aerosols on surface precipitation from clouds: an attempt at classification. *J. Atmos. Sci.* **65**: 1721–1748.

Khain A, Pokrovsky A. 2004. Simulation of effects of atmospheric aerosols on deep turbulent convective clouds using a spectral microphysics mixed phase cumulus cloud model. part ii: Sensitivity study. *J. Atmos. Sci.* **61**: 2983–3001.

Khain A, Rosenfeld D, Pokrovsky A. 2001. Simulating convective clouds with sustained supercooled liquid water down to −37.5 °C using a spectral microphysics model. *Geophy. Res. Lett.* **28**: 3887–3890.

Khain A, Rosenfeld D, Pokrovsky A. 2005. Aerosol impact on the dynamics and microphysics of deep convective clouds. *Quart. J. Roy. Met. Soc.* **131**: 2639–2663.

Koren I, Martins JV, Remer LA, Afargan H. 2008. Smoke invigoration versus inhibition of clouds over the amazon. *Science* **321**: 946–949.

Lohmann U, Feichter J. 2005. Global indirect aerosol effects: A review. *Atmos. Chem. and Phys.* **5**: 715–737.

Lohmann U, Zhang J, Pi J. 2003. Sensitivity studies of the effect of increased aerosol concentrations and snow crystal shape on the snowfall rate in the arctic. *J. Geophy. Res.* **108**: 4341–4357.

Mapes BE, Houze Jr RA. 1992. An integrated view of the 1987 australian monsoon and its mesoscale convective systems. i: Horizontal structure. *Quart. J. Roy. Met. Soc.* **118**: 927–963.

May P, Allen G, Vaughan G, Connolly PJ. 2009. Aerosol and thermodynamic effects on tropical cloud systems during twp-ice and active. *Atmos. Chem. and Phys.* **9**: 15–24.

May PT, Bringi VN, Thurai M. 2011. Do we observed aerosol impacts on dsds in strongly forced tropical thunderstorms? *J. Atmos. Sci.* **68**: 1902–1910.

May PT, Mather JH, Vaughan G, Jakob C, McFarquhar GM, Bower KN, mace GG. 2008. The tropical warm pool international cloud experiment (twp-ice). *Bull. Amer. Met. Soc.* **89**: 632–645.

Morrison H, Curry JA, Khvorostyanov VI. 2005. A new double-moment microphysics parameterisation for application in cloud and climate models. *J. Atmos. Sci.* **62**: 1665–1677.

Morrison H, Grabowski WW. 2011. Cloud-system resolving model simulations of aerosol indirect effects on tropical deep convection and its thermodynamic environment. *Atmos. Chem. and Phys.* **11**: 10 503–10 523.

Piani C, Durran D, Alexander MJ, Holton JR. 2000. A numerical study of three–dimensional gravity waves triggered by deep tropical convection and their role in the dynamics of the qbo. *J. Atmos. Sci.* **57**: 3689–3702.

Press WH, Flannery BP, Teukolsky SA, Vetterling WT. 1993. *"numerical recipes in c: The art of scientific computing"*. "Cambridge University Press", 2 edn.

Ramage CS. 1968. Role of a tropical "maritime continent" in the atmospheric circulation. *Mon. Wea. Rev.* **96**: 365–370.

Roberts NM, Lean HW. 2008. Scale-selective verification of rainfall accumulations from high resolution forecasts of convective events. *Mon. Wea. Rev.* **136**: 78–97.

Rogers RR, Yau MK. 1989. *A short course in cloud physics*, *"International series in natural philosophy"*, vol. 113. "Pergamon press", 3 edn.

Rosenfeld D. 1999. Trmm observed first direct evidence of smoke from forest fires inhibiting rainfall. *Geophy. Res. Lett.* **26**: 3105–3108.

Rosenfeld D, Woodley WL. 2000. Deep convective clouds with sustained supercooled liquid water down to −37.5 °C. *Nature* **405**: 440–442.

Rosenfeld D, Woodley WL. 2001. Pollution and clouds. *Physics World, Institute of Physics* **Feb 2001**: 33–37.

Saito K, Keenan T, Holland G, Puri K. 2001. Numerical simulation of the diurnal evolution of tropical island convection over the maritime continent. *Mon. Wea. Rev.* **129**: 378–400.

Seifert A, Beheng KD. 2005. A two moment cloud microphysics parameterisation for mixed phase clouds. part ii: Maritime vs continental deep convective storms. *Meteor. and Atmos. Phys.* **in press**.

Skamarock WC, Klemp JB, Dudua J, Gill DO, Barker DM, Duda MG, Huang XY, Wang W, Powers JG. 2008. A description of the advanced research wrf version 3. Technical report, NCAR.

Swann HA. 1998. Sensitivity to the representation of precipitating ice in crm simulations of deep convection. *Atmos. Res.* **48**: 415–435.

Tao WK, Li X, Khain A, Matsui T, Lang S, Simpson J. 2007. Role of atmospheric aerosol concentration on deep convective precipitation: cloud-resolving model simulations. *J. Geophy. Res.* **112**: D24S18, doi:10.1029/2007JD008 728.

Tao WK, Simpson J. 1984. Cloud interactions and merging: Numerical simulations. *J. Atmos. Sci.* **41**: 2901–2917.

Topping DO, McFiggans GB, Coe H. 2005a. A curved mult-component aerosol hygroscopicity model framework: Part 1 - inorganic compounds. *Atmos. Chem. and Phys.* **5**: 1205–1222.

Topping DO, McFiggans GB, Coe H. 2005b. A curved multi-component aerosol hygroscopicity model framework: Part 2 - including organic compounds. *Atmos. Chem. and Phys.* **5**: 1223–1242.

Twomey S. 1959. The nuclei of natural cloud formation: the supersaturation in natural clouds and the variation of cloud droplet concentration. *Geofis pura et appl.* **43**: 243–249.

van den Heever SC, Cotton WR. 2007. Urban aerosol impacts on downwind convective storms **46**: 828–850.

van den Heever SC, Gustavo GC, Cotton WR, DeMott PJ, Prenni AJ. 2006. Impacts of nucleating aerosol on florida storms. part i: Mesoscale simulations. *J. Atmos. Sci.* **63**: 1752–1775.

van den Heever SC, Stephens GL, Wood NB. 2011. Aerosol indirect effects on tropical convection characteristics under conditions of radiative-convective equilibrium. *J. Atmos. Sci.* **68**: 699–718.

Vaughan G, Schiller G, MacKenzie AR, Bower KN, Peter T, Schlager H, Harries NRP, May P. 2008. Scout-o3/active. *Bull. Amer. Met. Soc.* **89**: 647–662.

Williams ER, Rutledge S, Geotis SG, Renno N, Rasmussen RM, Rickenbach T. 1992. A radar and electrical study of tropical 'hot towers'. *J. Atmos. Sci.* **49**: 1386–1395.

Wilson J, Carbone R, Tuttle JD. 2001. Tropical island convection in the absence of significant topography. part ii: Nowcasting storm evolution. *Mon. Wea. Rev.* **129**: 1637–1655.

Zhang H, McFarquhar GM, Saleeby SM, Cotton WR. 2007. Impacts of saharan dust as ccn on the evolution of an idealized tropical cyclone. *Geophy. Res. Lett.* **34**: L14 812, doi:10.1029/2007/GL029 876.

Zhu M, Connolly PJ, Vaughan G, Choularton TW, May P. 2012. Numerical simulation of tropical island thunderstorms (hectors) during the active campaign. *Met. Apps.* **accepted**.